THERMAL MANAGEMENT AND SOLIDIFICATION CHARACTERISTICS IN HIGH PERFORMANCE ALUMINUM CASTING

THERMAL MANAGEMENT AND SOLIDIFICATION CHARACTERISTICS IN HIGH PERFORMANCE ALUMINUM CASTING

By Satyam Sharma, B.Tech. IIT-BHU

A Thesis Submitted to the School of Graduate Studies in Partial Fulfillment

of the Requirements for the Degree Masters of Applied Science

McMaster University

McMaster University MASTERS OF APPLIED SCIENCE (2016) Hamilton, Ontario

TITLE: Thermal Management and Solidification Characteristics in High Performance Aluminum Casting
AUTHOR: Satyam Sharma
SUPERVISORS: Dr. Joseph McDermid, Dr. Joseph Kish, Dr. Sumanth Shankar
NUMBER OF PAGES: xiii, 96

Acknowledgements

I would like to acknowledge Automotive Partnerships Canada, Fiat Chrysler Automotive Group, Nemak, Haley Industries and CanMaterials for the funding and the technical support received.

I gratefully acknowledge my supervisors, Dr. Joseph McDermid, Dr. Joseph Kish and Dr. Sumanth Shankar for their support and guidance.

I would like to thank Dr. Kifah Takrouri, for his help and suggestions in conducting the experiments.

Finally, I'm thankful to my family for their continuous unwavering support and endless love.

Abstract

Weight reduction in automobiles is amongst the most economical ways of reducing greenhouse gas emissions and increasing fuel efficiency. The recently invented ablation casting process is a novel technique of producing high performance light weight parts which meet this objective. In this technique a water jet demolds the water soluble sand mold and subsequently impinges upon the solidifying metal, thereby producing high cooling rates in the casting which in turn leads to microstructural refinement and higher mechanical properties.

The objective of this study was to develop a comprehensive understanding of the effect of various parameters involved in the casting of a thin walled part using the HiPerMag casting process for the wrought aluminum alloy AA 7050.

The study is divided into three major parts that deal with the composition of the sand binder system, optimization of the sand mold thickness, various aspects of the water jet parameters and the desired microstructural parameters which will result in a defect free part.

In first phase of the study, sand mold properties such as the green and dry strengths of the water soluble sand binder system used in the study were tested to ensure that they meet the molding requirements. An average green strength of 160 kPa and an average dry strength of 3825 kPa were found for the water soluble sand binder system. These

values were similar to those reported in the literature for clay bonded sands and were sufficient to make molds for casting in the current study.

Secondly, a heat transfer model was developed to find a minimum mold thickness required to design a mold for the HiPerMag casting process such that the liquid metal remained sufficiently insulated before being quenched. Based on the model, for a mold with a cope thickness of 12.9 cm, the heat flux losses to the surroundings were reduced by up to 90 % versus a case where a thinner mold was used.

In addition, an analytical solution was derived for the mold thickness problem from which it was found that at a distance of 10 cm from the mold cavity there was a negligible increase in temperature of the sand at that location at large times.

Further, the minimum mold thickness was determined based on the temperature profile in the sand mold during the HiPerMag casting process. This study showed that a thin mold of about 2 cm thickness was sufficient to provide insulation to the hot metal during the HiPerMag casting process.

Thirdly, it was found that, based on cooling curve data and microstructural analysis, that a jet spacing of 15.3 cm and a time delay of 7.4 s between successive jet activations starting from the farthest jet (located near the edge of the casting), was necessary to obtain a single solidification front throughout the casting. This also ensured that grain size variation in the casting was less than 10 μm for having uniform mechanical properties.

Also, it was found for a thin walled casting, the amount of solid present in the solidifying casting at the time of water jet impingement had a negligible effect on the movement of the solidification interface.

Finally, the effect of jet momentum on surface defects was examined. It was determined that the maximum jet momentum resulting in no surface defects at temperatures close to the liquidus for Al AA 6061 alloy was approximately 2 kg.m/s.

Table of Contents:

List of Figures

List of Tables

Nomenclature

Symbol	Unit	Description
h_g	$W/m^2.K$	Heat transfer coefficient of the air gap
h	$W/m^2.K$	Heat transfer coefficient between mold and surroundings
k	W/m.K	Thermal conductivity of the sand
P	Pa	Waterjet Pressure
ρ	kg/m^3	Density
t	s	Time

Abbreviations

Abbreviation	Meaning
AFS	American Foundry Society
MIG	Metal Inert Gas
HPDC	High Pressure Die Casting
MT	Mold Thickness
OEM	Original Equipment Manufacturer
OP	Overlapping Percentage of Multijets
SDAS	Secondary Dendrite Arm Spacing
SOD	Standoff Distance
SRR	Sand Removal Rate
UTS	Ultimate Tensile Strength
WJM	Waterjet Momentum
YS	Yield Strength
POP	Plaster of Paris
BIW	Body in White

Chapter 1: INTRODUCTION

Currently 95 percent of energy needs for USA's transportation sector are met by petroleum, 60% of which is imported [1]. The United States Department of Energy and the United States Council of Automotive Research have worked through their Freedom Car and Fuel Partnership (FC&FP) initiatives since 2002 to develop new automotive technologies to reduce dependence on imported petroleum [1]. The predecessor to the (FC&FP) was the PGNV (Partnership for a New Generation of Vehicles) which existed until 2002 [1].Some of the development efforts that translated into OEM production through the PGNV were the use of Al sheet forming and glass-fiber-reinforced polymer-matrix composites (glass-FRPMCs) for automotive weight reduction [1] The main thrust area of the (FC&FP) was the use of Mg and carbon-FRPMCs for the long term and Al and advanced high-strength steels (AHSSs) for the medium term. With the next generation of hybrid and fuel cell powertrains that are heavier and more expensive per unit power being expected to replace conventional gasoline based powertrains, research in to lightweight, high performance materials is currently being carried out for long term benefits. Table 1 shows a comparison of various lightweight materials. It can be observed that parts made of aluminum offer a 40-60% mass reduction when used in place of parts made using mild steel or cast iron [1].

Table 1: Comparison of lightweight materials [1]

Lightweighting material	Material replaced	Mass reduction (%)	Relative Cost (per part)*
High Strength Steel	Mild Steel	10	1
Aluminum (Al)	Mild Steel, Cast Iron	40 – 60	1.3 – 2
Magnesium	Steel or Cast Iron	60 – 75	1.5 – 2.5
Magnesium	Aluminum	25 – 35	1 – 1.5
Glass FRP Composites	Steel	25 – 35	1 – 1.5
Graphite FRP Composites	Steel	50 – 60	2 – 10+
Al Matrix Composites	Steel or Cast Iron	50 – 65	1.5 – 3+
Titanium	Alloy Steel	40 – 55	1.5 – 10+
Stainless Steel	Carbon Steel	20 – 45	1.2 – 1.7

Weight reduction is amongst the most effective ways of reducing automotive greenhouse emissions and increasing fuel economy. For example, for every 10 % weight reduction there is generally an increase of 7 % in fuel economy [2]. Currently the body in white (BIW), which consists of a welded steel space frame accounts for 99.9 % of the cars produced. About 0.1 % are constructed with aluminum frames and 0.01 % with carbon fiber composites [2]. Generally, the BIW accounts for approximately 20 % of total vehicle mass [2].

The relatively low cost of steel, its wide range of mechanical properties and ease of manufacture makes it a top choice as an automotive structural material. In recent times, the proportion of ferrous metals per car has been reduced due to the use of aluminum in engine castings, wheels, closures (e.g. the current Ford F150) and suspension components and plastics in the hood and in bumper moldings [2].

Ghassemieh [2] has compared steel, aluminum, magnesium and composites for their relative applicability as automotive materials. Advanced high strength steels and high

strength low alloy steels offer up to a 19 % reduction in weight and demonstrate superior strength and crashworthiness than conventional steel auto bodies. Also AHSS's with significant retained austenite–the so called Transformation Induced Plasticity or TRIP steels– with a specific strength similar to or superior than aluminum possess high positive strain rate sensitivity, which leads to enhanced crash performance [2].

Aluminum alloys also offer potential weight saving benefits when used in automotive parts, which is one of the reasons aluminum alloy usage per vehicle is expected to rise from 110 kg in 1996 to 340 kg in 2015 [2]. Examples of automotive applications of aluminum castings include power train components such as piston cylinder heads and intake manifolds. Aluminum castings are also being used in decorative wheel rims, for brackets, brake components, suspension components (e.g. control arms, supports), steering components (e.g. air bag supports, steering shafts, knuckles, housings, wheels) and instrument panels. Wrought aluminum alloys are being used in applications where high mechanical properties are required such as forged wheels and bumper reinforcements, air bag housings, pneumatic systems, sumps, seat frames, and side impact panels [2].

Magnesium is 33 % less dense than aluminum and 75 % less dense than steel/cast iron. However, pure magnesium has a lower elastic modulus, ultimate tensile strength, fatigue strength and creep resistance versus aluminum and is therefore alloyed to

improve its properties [2]. However, Mg alloys such die cast AM50 or AM60 can achieve elongations of 20 %, leading to higher impact strength versus Al die cast alloys such as Al380 [2]. Mg alloys with rare earth elements such as thorium, cerium, and zirconium are made for high temperature application due to their superior creep resistance and have been successfully employed by BMW for engine block applications [2]. A disadvantage of Mg alloys over aluminum or advanced steels is their high reactivity and poor galvanic corrosion resistance. Furthermore, during casting, machining and grinding, suitable protective gases should be used and precautions need to be taken to prevent fire hazards due to the energetic oxidation of magnesium and its vapors [2].

Polymers composites have been used in the automotive industry since they first appeared in the 1953 Corvette. Composites offer benefits such as reduced weight, design flexibility, corrosion resistance and anisotropy. The major disadvantages which restrict their use are high costs, low production rates and concerns about recyclability and end of life disposal [2].

1.1 Motivation

It is evident from the literature that lighter materials such as aluminum and magnesium offer potential weight saving benefits for automotive structures. In addition, thin walled parts offer additional weight saving benefits on account of their high specific strength (strength at failure/density) and specific stiffness (elastic modulus/density) of these

materials. However, there are numerous challenges involved in the casting of thin walled high performance castings such as the filling of the mold, design of the gating system and achieving the required high mechanical property targets. Conventional sand castings cannot meet these stringent requirements for the next generation of high performance parts due to high percentage of associated defects, such as gas and shrinkage porosity, and low solidification/production rates which accompany such castings.

Ablation casting technology has received widespread attention from the automotive industry as a novel technique to manufacture high performance parts. The process not only reduces defects such gas and shrinkage porosity but also enhances mechanical properties due to directional solidification and finer microstructure.

The HiPerMag casting process involves making a sand mold with a water soluble sand binder system and then rapidly de-molding it using high pressure water jets to achieve high cooling rates in the casting. These high cooling rates result in grain refinement of the primary alpha (Al) phase in the microstructure, leading to high mechanical properties relative to conventionally cast alloys. The primary motivation of this thesis is to explore selected process parameters critical to the HiPerMag casting process and their effect on dependent variables such as mold thickness, casting microstructure and surface defects.

In the course of the past few years, several studies have been conducted on the ablation casting process and articles published. A review of these studies is presented in Chapter 2. Chapter 3 presents the objectives of the study and the project plan. Chapter 4 describes the experimental methodology which includes the setup, procedures and analysis techniques used in the project. Chapter 5 presents the experimental results and discusses them within the context of the existing literature and, finally, Chapter 6 provides summative conclusions of the study.

Chapter 2: LITERATURE REVIEW

The literature relevant to this project was broadly categorized as follows:

2.1 SAND BINDER SYSTEM

2.2 ABLATION CASTING PROCESS

2.3 HOT TEARING

2.4 ESTIMATION OF SAND REMOVAL RATE

2.1 Sand binder system

Commercially available binders can be classified into two types: organic and inorganic, where organic binders include resins and oils which are not water soluble after curing and usually form gases during the casting process. Common inorganic binders are sodium silicates, plaster of Paris, and phosphates. Generally inorganic binders are not gas producing during casting. However, inorganic binders are associated with problems relevant to the collapsibility/removability of the cores after casting. This problem can be solved by using a combination of a phosphate binder with clay. The binder system currently under investigation, a borax-phosphate salt based binder, cures by the evaporation of water to give a strong bond with no detrimental fumes produced during casting [3].

Bentonite is an aluminium phyllosilicate, essentially an impure clay consisting mostly of montmorillonite [6]. Montmorillonites (also called a 2:1 mineral) have a three layered

structure consisting of one sheet of aluminum hydroxyl octahedral sandwiched between two sheets of silicon-oxygen tetrahedra as shown in Figure 1. These sheets are joined by shared oxygen atoms [4]. In this structure aluminum atoms are partially substituted by magnesium or iron atoms leading to a small net negative charge within the structure. This charge is balanced by absorption of exchangeable cations such as Na^{+}/Ca^{2+} between adjacent subunits, also referred to as platelets. During hydration, a large amount of water is absorbed in the interlayer spaces as a result of hydrogen bonding between the water molecules and platelet surfaces leading to swelling properties observed in bentonite [5]. A high quality sodium bentonite has been reported to have about 25-50 water layers [6]. The number of layers of water molecules depends on the moisture content of the clay and decreases with decreasing moisture content (i.e. with increased mulling). The maximum strength obtained for a particular moisture level depends on the layered structure. Too many layers cause slip and reduce strength. Also just a single layer being bonded too tightly to a crystal cannot hold the binder grains strongly, also resulting in low strength [7].

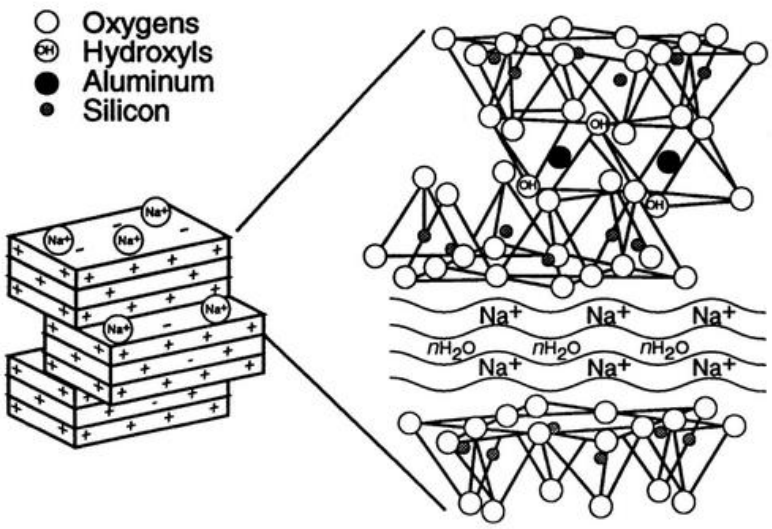

Figure 1: Crystalline structure of sodium montmorillonite showing interlamellar water layers [8]

In order to be useful as a binder in sand casting, bentonites require thorough mulling in order to properly coat the sand grain surfaces and prevent any tendency for the clay and water additions to form agglomerates, which can lead to variations in the rammed strength of the mixture.

Normally, 6.0 wt. % bentonite in sand mixture is required for sufficient coverage of the sand grains by the bentonite and adequate binding of the sand grain surfaces. Bentonite additions below this level are considered to be insufficient resulting in improper coating of the sand grains [9].

Based on its moisture content, the strength of clay-bonded sand can be assessed in two states or conditions; namely, green strength and dry compressive strength. Green

strength refers to the compressive strength when the sand is in a moist state. The sand mixture must possess sufficient green strength so it can retain its shape when pattern is removed. Dry strength refers to the compressive strength of the sand in the dry condition. In this case, the mold is dried by baking it in a furnace in order to remove the water. The sand mix should possess an optimal dry strength such that the mold can not only withstand the hot metal erosion during pouring and filling of the mold, but is also collapsible during shakeout [10].

Figure 2 a) shows the effect of mulling time on the green compressive strength. It can be seen that the green strength increased with mulling time until a maximum was reached, after which it remained relatively constant. Figure 2 b) shows the effect of sand grain size and moisture content on green strength, from which it can be seen that the green strength increased with decreasing the sand grain size. Also, the green strength increased initially with moisture content until attaining a maximum, after which it decreased [11].

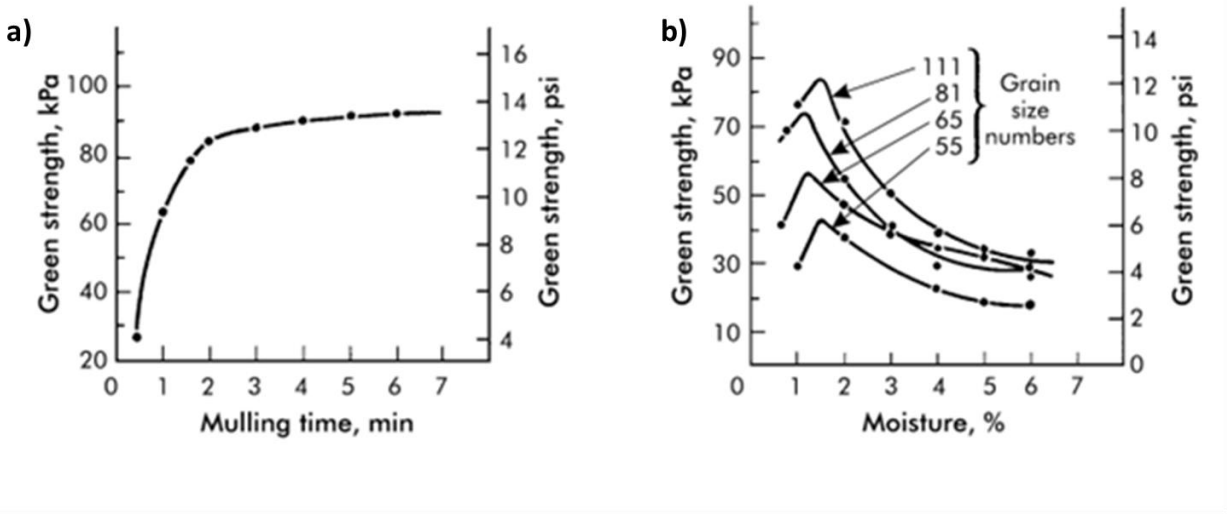

Figure 2: a) Effect of mulling time on green strength b) Effect of moisture content and particle size on green strength [11]

Green compressive strengths of 146.9 kPa (21.3 psi) and 96.52 kPa (14 psi) have been reported for a 8 wt. % calcium bentonite bonded AFS 85 silica sand mixture containing 3.2 wt. % and 4.6 wt. % water, respectively, after mulling for 10 minutes. In a similar case, reducing the bentonite to 6 wt. % whereas keeping the mulling time and the sand grain size unchanged, resulted in a green strength of 68.95 kPa (10 psi) at 2.6 wt. % water [12]. In an another study by Heine et al. [13], for an AFS 85 silica sand mixture containing 6 wt. % calcium bentonite, a green strength of 103.42 kPa (15 psi) and a dry strength of 413.68 kPa (60 psi) were reported for a 3.0 wt.% moisture level under a fully mulled condition.

From the above literature it is clear that per industry practice, a sand mixture containing 6-8 wt. % calcium bentonite, which has an optimum water percentage of about 3 wt. % and is sufficiently mulled will yield a green strength of approximately 137 kPa (20 psi)

and a dry strength of 413 kPa (60 psi). These are considered to be adequate for handling during molding operations.

2.2 Ablation casting process

The "ablation" casting technology aims to remove the aggregate mold held together with an environmentally friendly, water soluble inorganic binder using a water jet, which impinges on the mold to dissolve it away, thus allowing water to come into direct contact with the casting. Using this technique, high cooling rates in the casting can be achieved and directional solidification enhanced, hereby, leading to uniform properties. In addition to the mold, complex internal cores can be eliminated, while providing a high cooling rate to the casting [14].

In a previous study using the ablation casting technique [14], an automotive steering knuckle shown in Figure 3 a) was cast using Al alloy A356.2. The mold was made using AFS 60 silica sand bound with sodium silicate. The casting was poured at a temperature of 720°C. After pouring the mold was subjected to an ablation jet curtain (shown in Figure 3 b) with a water temperature of 65°C applied to the furthest arms of the casting progressing upwards along its length. After casting, a standard T6 heat treatment was applied. Temperature gradients on the order of 60 K/mm were reported to be have been achieved [14].

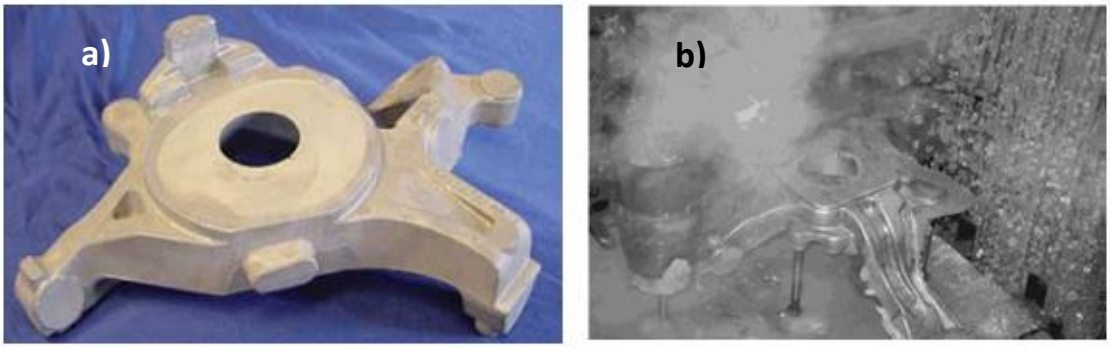

Figure 3: a) Cast automotive steering knuckle b) Water jet positions and sprue [14]

The optical microstructures of a test casting taken from a steering knuckle cast without and with ablation are shown in Figure 4 a) and b); respectively, and are typical of an un-modified Al-Si eutectic. Typical ablation-cast structures are shown in Figure 4 b) and show that the dendrite arm spacing has been significantly refined [14]. After heat treatment and aging, the mechanical properties were found to improve significantly. A mean yield and tensile strength of 233 MPa and 321 MPa respectively and an elongation of 12.4 % were reported from the samples taken from the cast knuckle [14].

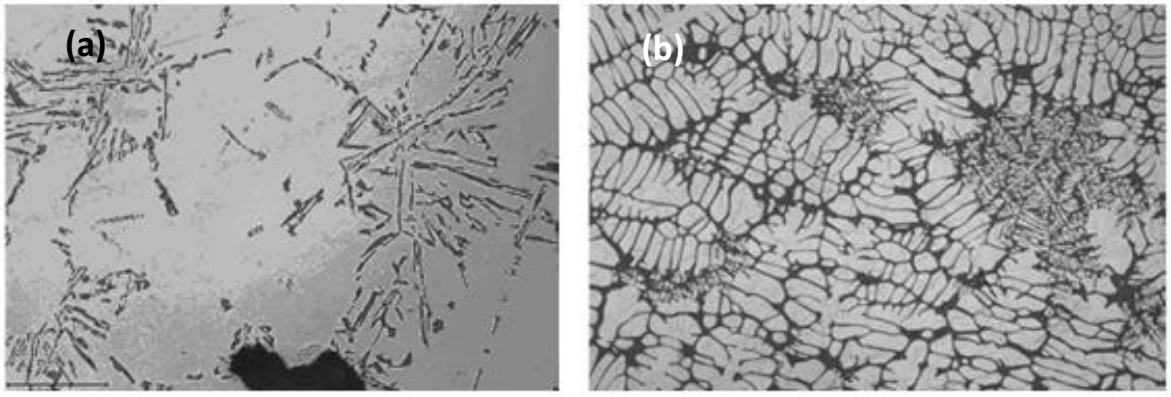

Figure 4: a) Microstructure without ablation b) Microstructure with ablation [14]

Apart from the merits of the ablation casting process mentioned in the above paper [14], the patent [15] discusses the effect of cooling rate on the secondary dendrite arm spacing (SDAS), as shown in Figure 5 below.

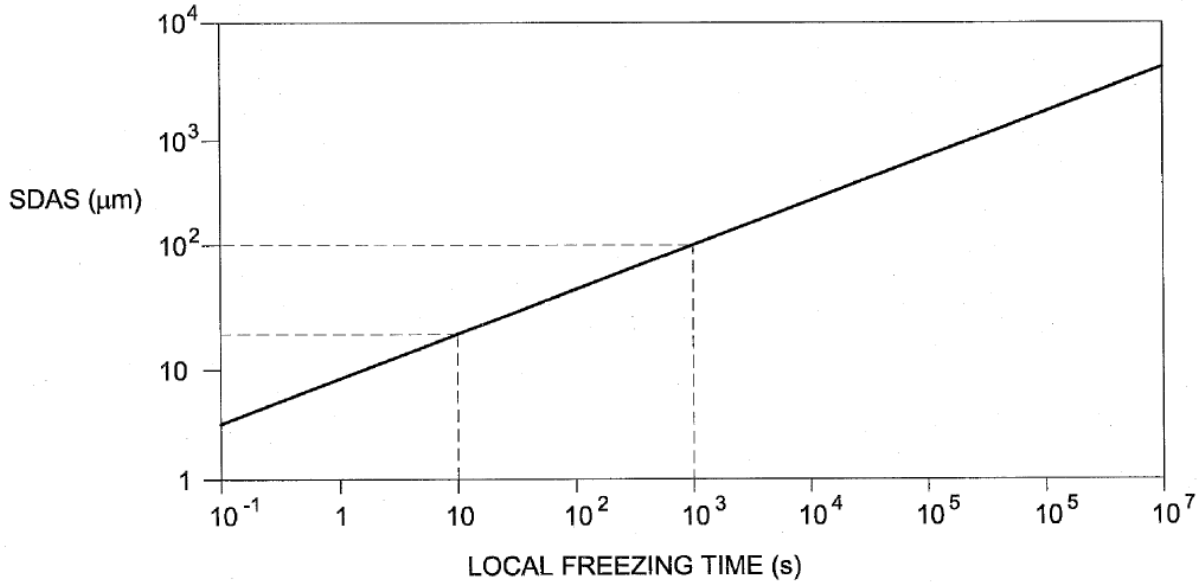

Figure 5: Dendrite arm spacing vs. solidification rate [15]

From Figure 5 it can be seen that by reducing the freezing time by 100 times, the SDAS was reduced by a factor of five (i.e. from 100 μm to 20 μm). Although the volumetric flow rate, pressure, and temperature of the coolant were identified as important parameters, no effort has been made to study or discuss their effect on dependent parameters such as grain size, mechanical properties etc. Also, the solidification model for the prediction of grain size was rudimentary and lacked precision.

In another study by Bahlooli et al. [16], it was stated that ablation casting is a process where higher cooling rates can be achieved versus conventional sand casting and which

reduce the primary and secondary dendrite arm spacing, leading to a more homogenized microstructure and improved mechanical properties. In the conventional sand casting process, when melt is poured into a mold, the solidification front moves from the wall towards the center of the mold. When this outer shell solidifies, it contracts leading to an air gap between the mold and the casting, which in turn reduces the rate of heat extraction, thereby reducing the mechanical properties of the casting. The objective of the ablation casting process is to dissolve the mold, thereby eliminating the air gap and hence cooling the solidifying metal directly by water impingement and leading to improved properties. In the study of Bahooli et al. [16], the feedability, porosity, general microstructure and SDAS of an A356 aluminum casting were investigated. The ablation cast samples were found to have better feedability (i.e. ability to able to feed thick sections when they shrink during solidification), lower porosity and lower SDAS. In addition, the ablated specimens had a finer and more homogenous microstructure as compared with the non-ablated ones.

In this case the effect of the casting process on the properties of an L-shape aluminum casting was investigated by using two molds which were ablated and two which were not. An example of the L-shaped casting and its dimensions are shown in Figure 6 [16].

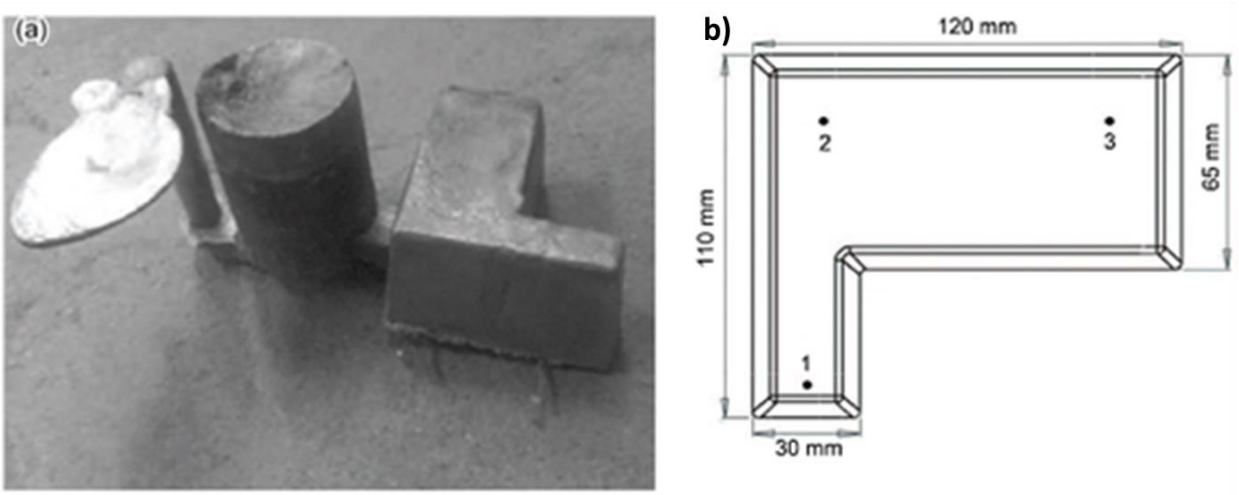

Figure 6: a) L shaped cast part b) Thermocouple locations [16]

The binding mixture consisted of 2.0 wt. % bentonite and 15.0 % clay added to silica sand. The melt was prepared at 750 °C, and the casting was poured at 710 °C. Three pairs of K-type thermocouple were placed in each mold at positions 1, 2 and 3 illustrated in Figure 6. The ablation casting process was established using of a water spray system. The water spray system was placed near thermocouple position 1 of the ablated molds, as shown in Figure 7.

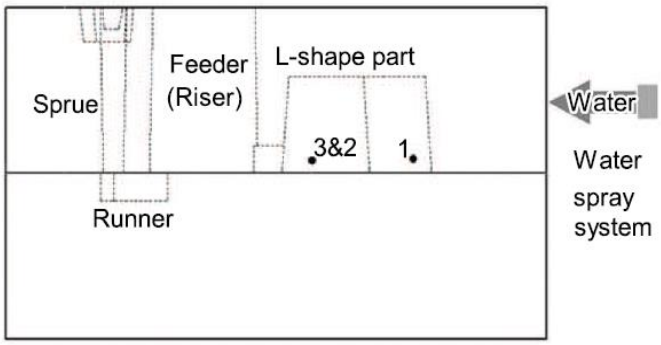

Figure 7: Schematic of feeder and location of water spray [16]

As previously mentioned, Bahooli et al. [16] stated that the ablated samples were found to have a finer and more homogeneous microstructure than the non-ablated ones. The authors also stated that within the cast part the SDAS was smaller by about 35 % in regions which were under the direct impingement of the water jets (i.e. with higher cooling rates) as compared to regions far from the jet. Furthermore, the regions directly impinged on by the water jet had lower porosity as compared to regions away from the water jet. The explanation of this was that the regions farthest from water jet were the last to solidify and, hence, captured the majority of the shrinkage [16].

The above paper explained the benefits of the ablation casting process over conventional casting and details concerning the experimental setup used in the study were provided. However, the meaning of the term “homogenous microstructure” was ambiguous in the contribution. A significant shortcoming of the study was that no micrographs were provided to quantitatively show the effect on casting porosity.

Weiss et al. [17] investigated the effect of ablation casting on Al-SiC metal matrix composites. Al-SiC composites have been widely used in brake rotors [17]. However, these composites are difficult to machine due to the settling of the hard, higher density SiC particles during conventional sand casting. Al-SiC composites with graphite were used in the study as developed by Rohatgi et al. [18]. The addition of graphite resulted in a buoyancy neutral melt where both reinforcement phases remained suspended in

the liquid metal. The effect of ablation cooling on a hybrid Al-SiC composite containing 10 vol. % SiC and 4 vol. % Ni coated graphite was studied. A 40.64 cm x 20.32 cm plate shaped pattern with a thickness of 6.35 cm on the left and 3.81 cm on the right was cast. The alloy was mixed for 30 min before pouring at 732 °C. A patented Alotech/De Venne inorganic binder was used to make the ablation molds. The casting was subjected to ablation cooling starting from the thinnest section towards the thicker section. After casting, the ablation and conventional castings were solutionized at 538 °C for 12 hours followed by quenching in a 60 °C water bath. Tensile and metallography samples were cut from the castings and analyzed. Optical micrographs for samples with and without ablation are shown in Figure 8. It was found that the graphite and SiC particles were more evenly distributed in the ablation cast component. The dendrite arm spacing (DAS) was reduced from 62.5 μm in the conventionally sand cast component to 50.3 μm in the ablation cast component and resulted in a 35% decrease in solidification time. However, significant porosity was reported in both the conventional and ablation cast components. Higher mean tensile strengths of 249 MPa was found in the ablation cast components as compared to conventional sand cast components which had a tensile strength of 219 MPa. It was found that during solidification, the particulate reinforcements (SiC and graphite) were pushed by the primary alpha dendrites into the last solute rich freezing zones. The increased solidification rates in the ablation cast component decreased the settling of the reinforcement in addition to refining the

dendritic cell size. The dependence of dendrite cell size on cooling rate is shown in Figure 9.

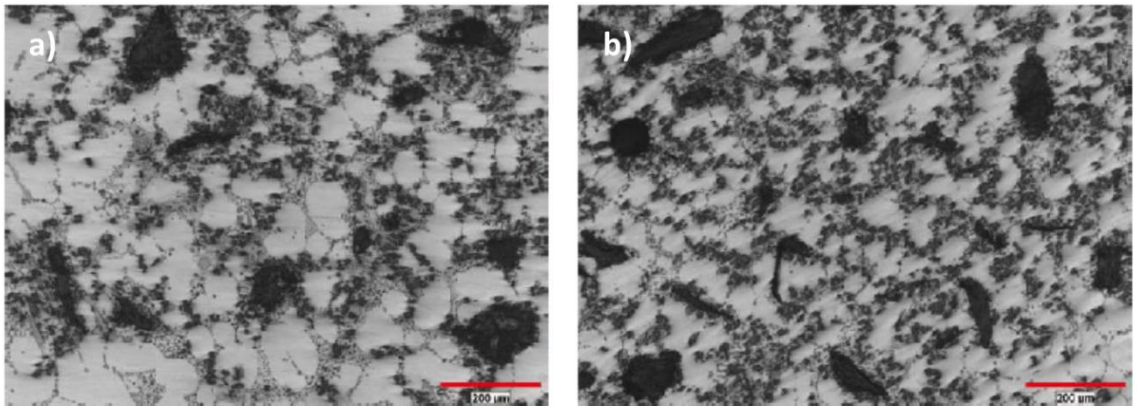

Figure 8: a) Conventionally cast composite b) Ablation cast composite showing evenly distributed SiC particles [19]

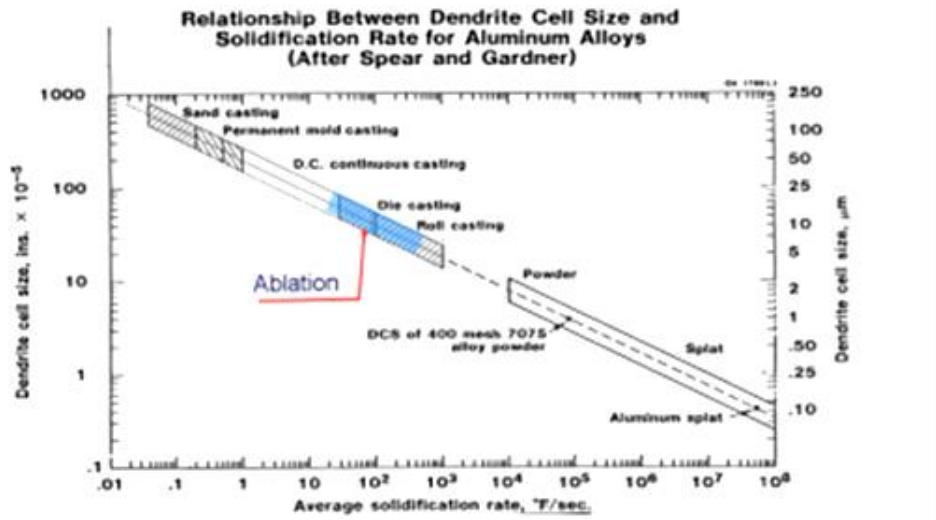

Figure 9: Ablation cooling rates and dendrite cell size compared to conventional casting methods [19]

From the above study it is clear that the ablation casting process leads to significant benefits in terms of the homogenous distribution of reinforcement and dendrite cell refinement leading to higher and uniform mechanical properties. The study provides

details concerning mold design, casting procedure and microstructure. However, no details of the jet parameters such as location, momentum, spray pattern etc. were provided or discussed. Also, the reason for no significant difference in porosity in the conventional versus ablation cast components was attributed to poor gating design, which is misleading as previous studies have reported significant reduction in porosity in ablation cast components as compared to conventional cast components.

Tiryakioglu et al. [20] studied the fatigue life of parts produced using the ablation casting process and compared it with forged and sand cast A356. In Al alloys, fatigue failure cracks are known to originate from defects such as inclusions and pores. Due to the low density of aluminum, its oxide films tend to remain suspended in the melt and form pores or cracks in the solidified metal. The fatigue life of a component is increased significantly when the density of these defects is minimized. The ablation casting process reduces the density of defects and also minimizes their size due to its high solidification rates [20].

The military handle shown in Figure 10 was cast using the ablation casting process using an AA 6061 wrought Al alloy. After casting, parts were solution treated at 540 °C for 6 hours and the quenched in a water bath maintained at 63 °C. The castings were naturally aged for 12 hours and then artificially aged for peak hardness. Round fatigue specimen of gage diameter 5.03 mm and gage length 100 mm were machined from the

casting. Fatigue testing was carried out on a rotary bending fatigue testing machine at 100Hz (6000 revolutions per minute) at four different maximum stresses.

Figure 10: The military handle casting after Tiryakioglu et al. [20], showing the locations from which the specimens were excised

The microstructure consisted of 30-50 µm equiaxed grains. Very little porosity was observed in the ablation cast component as compared to the sand cast and forged components. Figure 11 shows a comparison of the fatigue properties of the ablation cast components with conventional sand cast components. From this, it can be seen the ablation cast AA 6061-T6 had a better fatigue resistance than conventional sand cast A356-T6 at the same maximum stress (Figure 11 a)). The properties of the ablation cast component were also compared with the forged AA 6061-T6 component. It was found that the forged component had a YS 52 MPa higher than that of the ablation cast component. The forged AA 6061 component had a higher fatigue life than the ablation cast component, as shown by the S-N curves in Figure 11 b) [20].

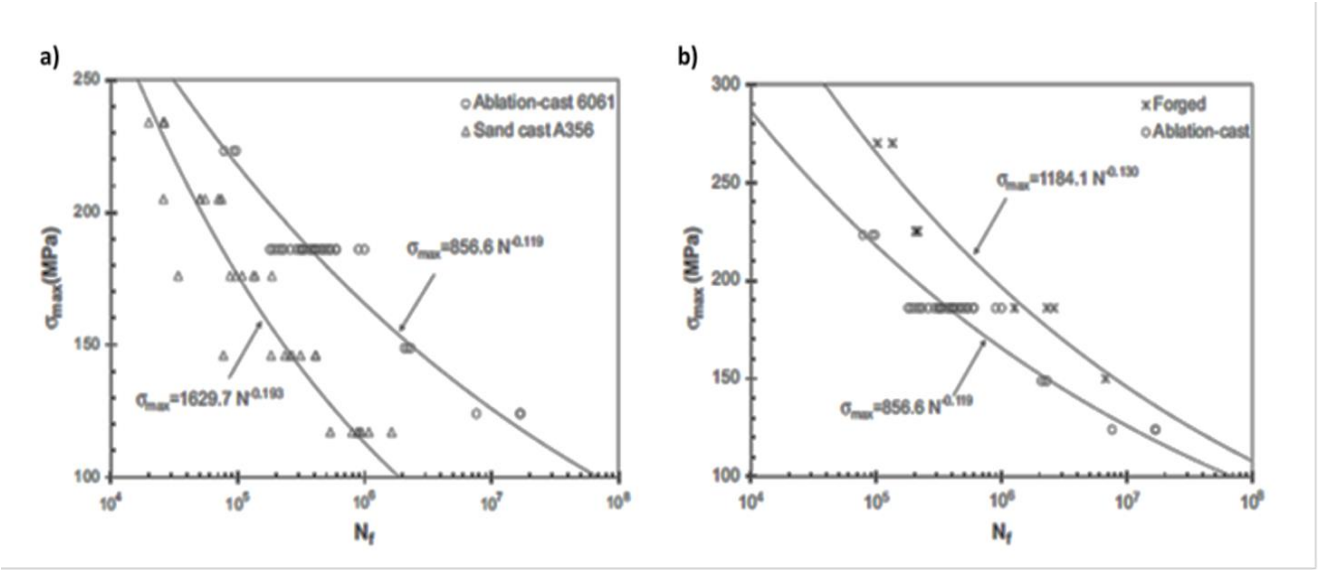

Figure 11: a) S–N curves for ablation cast AA 6061-T6 and sand cast A356-T6 b) S-N curves for ablation-cast and forged AA 6061-T6 [20]

Thomas et al. [21] conducted a feasibility study of the ablation casting process for steel castings and compared the process with conventional sand casting. A 101.6 cm long casting, 5.08 cm square cross section bar was cast with a riser at one end as shown in Figure 12. Silica sand with a phenolic no-bake binder was used to make the molds. The cope of the mold was removed after some time to spray the casting with water since the sand binder was not water soluble. The time for removal of the cope was calculated based on MAGMASOFT simulations as the time at which 80% of the metal had solidified at a depth of 1 mm below the casting surface. At 165 s after pouring, the cope was removed and sprayed with a low pressure garden hose at the end opposite to the riser. After the thermocouple at 15.2 cm (6 in.) from the end (refer to Figure 12) read 1400°C

the casting was assumed to have solidified at that section and the water spray was moved to the next location.

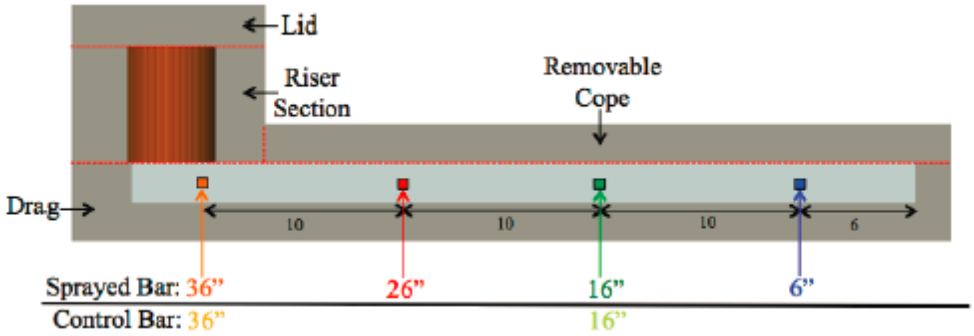

Figure 12: Geometry of the casting and thermocouple locations after Thomas et al. [21]

Large temperature gradients were obtained along the length of the bar which enhanced melt feeding, reduced centerline porosity and led to directional solidification. After casting, tensile specimens were machined with a gauge length of 7.62 cm and 2.54 cm radius. Tests were performed at a strain rate of $1x10^{-5}$ /s. The tensile and yield strengths increased from 540 MPa and 300 MPa for the conventionally cast component to 640 MPa and 420 MPa for the sprayed component. Ductility, however, was found to drop from 11 % to 7 %. It was believed that higher strength may have been due to the formation of martensite at the high cooling rates and hence the benefits on mechanical properties by the ablation casting process alone were not clear. However, the study showed that both the casting and heat treatment processes could be combined in the ablation casting process [21]. The radiography results showed that the sprayed bar had no centerline porosity as compared to the unsprayed bar which showed high centerline

porosity. Also, a high casting yield of 73.5 % (i.e. the volume of the bar divided by the total volume of the casting) was obtained by the ablation process since it required only one riser to feed the entire 101.6 cm long casting as compared to a conventionally cast component which would have required three risers in order to properly feed a casting of this size [22].

Prescenzi [23] utilized the ablation casting technique to manufacture six different body node castings for the 2016 Acura NSX. The all Al alloy space frame consisted of aluminum extrusions joined to sand cast aluminum nodes by MIG welding. The cast nodes were large (50.8 cm long) and were part of the energy absorption or crumple zone thus requiring a high UTS and elongation, which could not be met by conventional sand castings.

Prescenzi [23] compared various casting methods for their ability to meet the required specification for the part as shown in Table 2 below. Ablation casting was found to meet all the specified requirements such as the strength requirements, being able to cast thin walled sections, achieve high cooling rates and produce hollow sections.

Table 2: Comparison of casting processes for their ability to meet the product specification for the Acura body node (circle: met target, triangle: close to the specification minimum, X: did not meet target (HIP: Hot Isotactic Pressing, GDC: Gravity Die Casting, UHVHPDC: Ultra High Vacuum High Pressure Die Casting, LPDC: Low Pressure Die Casting, VRC: Vacuum Riserless Casting, PRC: Pressure Riserless Casting)) [23]

General Criteria							
Process	Yield / Tensile	Elong	Weld	Hollow	Wall T	Size	Volume / Invest
Sand + Chills and HIP	▲	▲	●	●	●	●	●
GDC	▲	x	●	●	▲	▲	●
UHVHPDC	●	▲	▲	x	●	▲	x
LPDC - VRC / PRC	●	▲	●	●	▲	●	▲/x

A Sr modified (0.01 wt. %) A356 alloy was used and was poured at 800°C. A refined eutectic microstructure was formed in the ablation cast parts. Mechanical properties sufficient to meet the requirements of the energy absorption zone: 190 MPa yield strength, 287 MPa tensile strength and 16.1 % elongation were achieved [23].

The above paper compared the various casting methods for producing lightweight Al body node castings for the 2016 Honda Acura NSX. It was determined that for a body node cast out of A356 alloy containing 0.01 wt. % Sr using the ablation casting process, the required shape, microstructure and target mechanical properties were achieved. A significant shortcoming of the study was that no details concerning the experimental setup and ablation jet parameters were provided.

2.3 Hot tearing

Hot tearing is one of most serious defect which occurs during casting.

Hot tearing is defined as a microscopic fissure which nucleates and grows inter-dendritically due to stresses generated during cooling at temperatures above the alloy solidus. The fundamental origin of the stresses which cause hot tearing is the volumetric contraction which occurs during the liquid to solid phase change which can lead to generation of strains within the material. These strains may lead to hot tearing if not accommodated by plastic deformation or movement of the solid or liquid. Various theories have been proposed to explain the mechanism of hot tearing in castings of which, the following three are most commonly referred to in the wider literature.

2.3.1 Theories of hot tearing

2.3.1.1 Shrinkage Brittleness theory

In this theory, hot tearing is defined as a "brittleness" which exists at temperatures above solidus due to the presence of liquid films between metallic crystals during solidification [24]. Most metals, with the exception to pure metals and eutectic alloys, possess a freezing range. As an alloy was cooled from a liquid state, primary dendrites form and start growing at the expense of the surrounding liquid. During the initial stages of solidification, the proportion of the liquid is large in comparison to the solid dendrites and the liquid is able to flow. However, during the later stages of solidification, dendrites impinge on each other leading to a coherent network, at which point the alloy

is unable to flow freely and behaves like a brittle solid. As the amount of liquid falls as solidification progresses, the strength of the alloy increases; however, fracture takes place at very low plastic deformations due to the poor elongation of the liquid films enclosing the solid crystals. An alloy is susceptible to hot cracking between the coherency point and the solidus and this temperature range is referred to as the brittle zone. For a given alloy, the morphology of dendrites is dependent on the temperature gradient between the solid and liquid phases, which in turn depends on the rate of heat extraction at the boundary (i.e. the cooling rate). It was found the percent eutectic necessary to heal the cracks increased with solidification rate. Hence, a slower cooling rate is believed to reduce the susceptibility to hot tearing [24]. The effect of the cooling rate on the minimum amount of eutectic required for healing is shown in Figure 13.

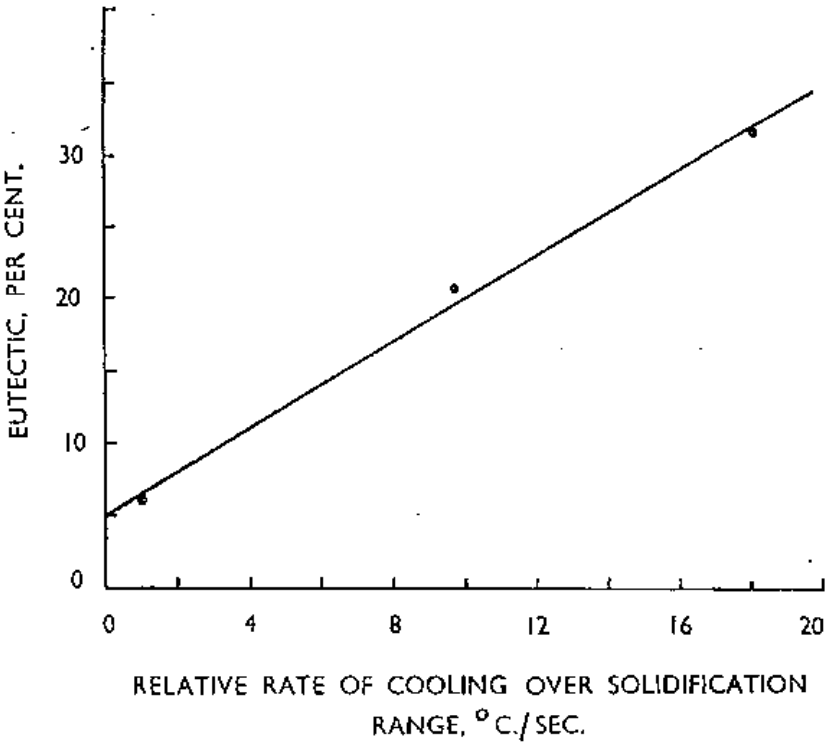

Figure 13: Relationship between rate of cooling over solidification range and proportion of eutectic necessary for healing after Pumphrey and Jennings [24]

2.3.1.2 Strain theory

Pellini [25] and his coworkers [26] proposed a theory which assumed that there was a liquid film stage in which all the solidified dendrites/grains are separated by a thin layer of liquid between them. A hot zone or a hot spot in a casting is a region which, due to its geometry or shape, is the last to solidify. The extension rate of the hot zone during liquid film stage determines whether a hot tear would occur or not. Further, the presence of segregating elements in the alloy causes these films to exist at temperatures below the solidus leading to a longer liquid film stage which results in an accumulation of extension leading to an increase in the tendency for hot tearing.

Long regions undergoing fast cooling develop high contraction stresses that require an extension of equal magnitude to be developed in adjoining hot spots, as shown in Figure 14. It was found that the narrower hot spots developed higher strains per unit volume, leading to an increased tendency for hot tearing. Hence, the width of a hot spot in a casting was an important factor for determination of the hot tearing tendency of a casting. Also, it was observed that low rates of cooling of a hotspot caused a build-up of extension strains which led to an increased tendency for hot tearing.

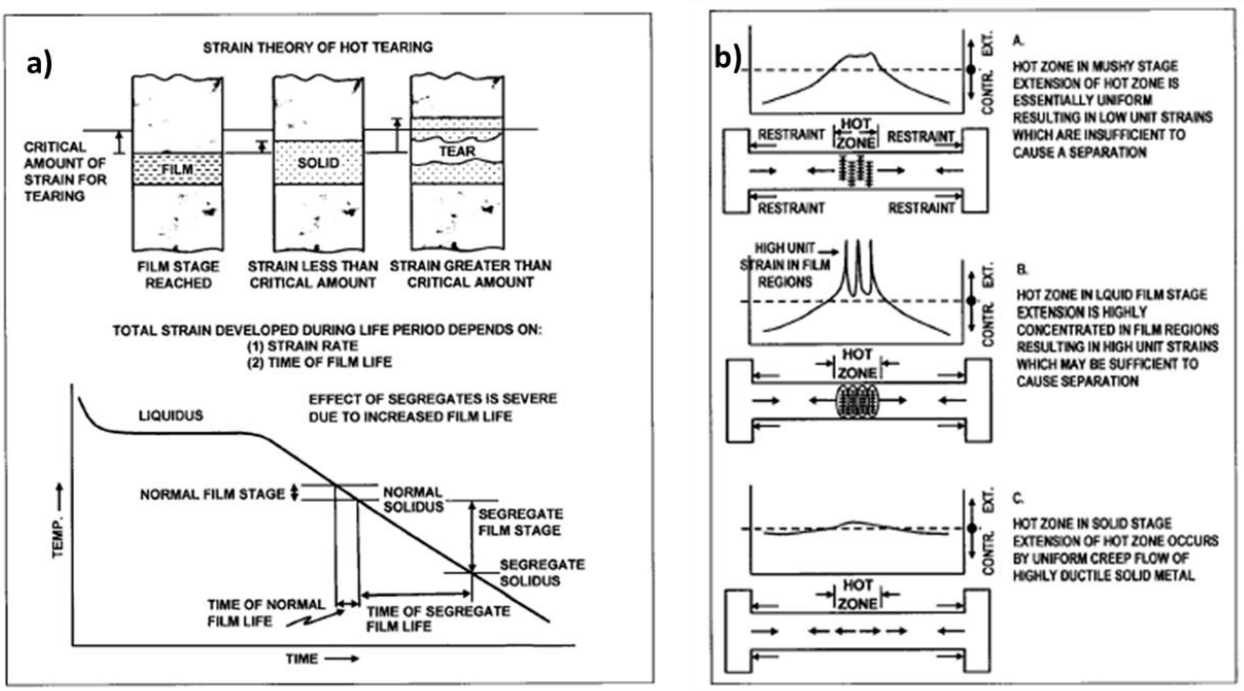

Figure 14:a) Diagram illustrating basic concepts of the strain theory b) Diagram showing the strain distribution within a hot spot [25]

2.3.1.3 Generalized theory

The generalized theory of Borland [27] suggests that the distribution of liquid at grain boundaries in the "critical solidification range" depended on the ratio of the solid-liquid interfacial energy to the grain boundary energy. The critical solidification range begins when an advanced solid crystal network has formed and there was no free flow of liquid between them and it extends upto the time when all of the liquid has solidified. The case where the entire surface of grain is covered with a liquid film is associated with a low ratio while a high ratio results in the liquid film being present only at the edges and corners of grains. The higher ratio results in a higher contact area between grains where more thermal stresses can be accommodated during cooling which leads to a lesser propensity to hot tearing.

The above literature provides an overview of various theories proposed to explain the mechanism for hot tearing. The shrinkage brittleness theory proposed that hot tearing occurs in the brittle temperature range after an interlocked network of dendrites is formed. The strain theory proposes that cracks occur when the film stage is reached and the strains are sufficiently high. The generalized theory combined both theories and further suggested that the shape of the liquid phase at the grain boundaries depended on the relative free energies of solid-liquid interface and grain boundary.

2.3.2 Process variables influencing hot tearing

Several process variables are known to strongly affect hot tearing, with the alloy eutectic content between the coherency point to the solidus (referred to as the effective solidification interval), the presence of trace elements in the alloy, the presence of hot spots in the casting arising from poor casting size and casting grain size being considered to be of importance.

Hot tearing was found to decrease with an increase in the amount of eutectic during the effective solidification interval. Three Al alloys containing 4.2, 6.6 and 11.2 wt. % Cu respectively were tested for their hot tearing tendency. It was observed that, as the amount of eutectic increased from the 4.2 wt. % Cu alloy to the 11.2 wt. % Cu alloy, the hot tearing tendency decreased [28].

Trace elements and impurities lead to an increase in hot tearing susceptibility as a result of increased solute segregation, which decreased the freezing temperature of the remaining liquid. For example, sulfur and phosphorus are known to promote hot tearing in steel [25].

The casting design also has a significant effect on hot tearing susceptibility by introducing high stress regions or “hot spots”. For example, as the metal solidifies in a thin section, it introduces shrinkage stresses in neighboring sections. The tendency to

hot tear can be reduced if the zones solidifying last are as long as possible in order to distribute the shrinkage stresses over a larger number of liquid films [25], [29].

During solidification, large columnar grains have limited mobility within the coherent network which reduces the ability of the liquid to feed properly into any inter-dendritic gaps. In addition, the coherency stage is reached earlier in the case of large columnar grains [30]. The majority of experimental studies have shown that grain refinement improved the casting's resistance to hot tearing due to an increase in inter-dendritic feeding and a reduction in liquid film thickness until the grain structure was cellular. Any further grain refinement led to an increase in hot tearing susceptibility due to decrease in the permeability of the mushy zone [31], [32].

Various articles have examined the effect of cooling rate of the casting on hot tear formation. In one of these studies on Mg alloys (AZ91D and AE42), it was reported that a high cooling rate leads to extensive branching of dendrites which hinders inter-dendritic feeding which caused an increase in tendency for hot tearing [33]. In another study on Al AA 2024 alloy, it was found that the hot tearing susceptibility decreased when moving from a low to a medium cooling rate (i.e. from 0.42 °C to 2.46 °C/s) and then increased again from a medium to a high cooling rate (i.e. from 2.46 °C/s to 17.45 °C/s). It was found that the fraction of eutectic phase at the grain boundaries increased with cooling rate. This phenomenon was reported to be dominant at lower cooling rates. However,

at higher cooling rates as those experienced in direct chill castings, the dendrite coherency point occurs at a lower solid fraction, therefore increasing the length of critical solidification interval which leads to an increase in hot tearing tendency [34].

In the above section, the influence of various parameters in hot tearing was discussed. The presence of trace elements in the alloy and hot spots in the casting increased the hot tearing susceptibility. The addition of grain refiner up to a limit reduced the hot tearing tendency, any further addition beyond this limit increased the hot tearing susceptibility.

2.4 Estimation of sand removal rate

It is clear from the literature that the ablation casting process consists of two stages: a rapid sand removal stage followed by a rapid cooling stage. In order to maximize the beneficial effects of the ablation process on the casting such as the refinement of grain size, lowering of shrinkage and gas porosity, the jet should impinge on the metal close to the liquidus and, therefore should be able to cut through sand quickly. For such a case, using a high momentum water jet is deemed to be necessary. However, if such a high momentum is continued in the cooling stage, it results in the formation of surface defects. In order to meet both the objectives of rapid sand removal and obtaining a part without surface defects, it is required to switch the momentum from a high value to a lower value during the HiPerMag casting process. For such purpose it is essential to

know the time a jet would take to cut through a given thickness of sand under various jet momentums.

Dursun [35] outline a procedure and developed an empirical relation for the sand removal rate based on various process parameters. However, as this thesis is under a publication ban at the time of the writing of this report, no further details can be provided here.

Chapter 3: OBJECTIVES AND PROJECT PLAN

The project has been divided into three phases:

PHASE I

- Develop a viable and optimized sand mold composition using a water soluble sand binder system.

PHASE II

- Design a suitable pattern and sand mold geometry to enable thin plate casting with Al alloys and subsequent rapid de-molding using a water jet.

PHASE III

- To predict the jet parameters such as jet spacing and activation timing required to have single solidification front throughout the part and to keep the grain size variation in the casting within a specific tolerance limit.

A flow chart summarizing the project methodology is provided in Figure 15.

The project was started with a literature review on available water soluble sand binder systems. After a binder was chosen, a 3D model of the part was built using the Autodesk Inventor software, the model was then used to machine the pattern and the mold box. With mold box and pattern ready, the next step was design an ablation casting (referred as HiPerMag casting henceforth) experiment. These experiments required inputs from module 2 of the project in form of sand removal rate at various jet momentums so that

the water jets could be timed precisely to impinge on the casting at a desired time delay and also from plate casting experiments to get important information such as number of jets to be used and their spacing such that a single solidification front could be obtained. Subsequently, the part was cast and visual inspection and microstructural analysis was carried out to validate the various models used in the study.

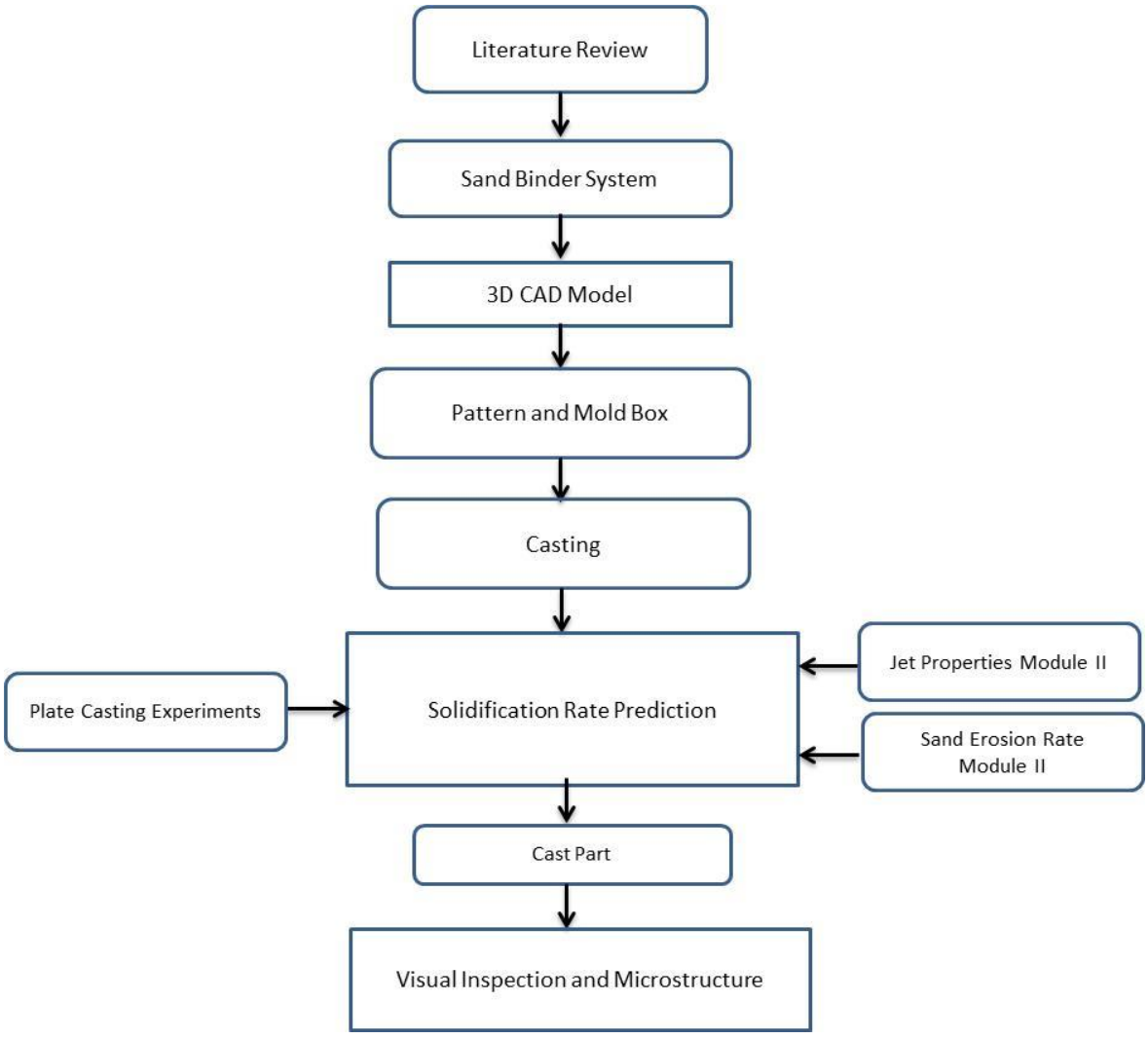

Figure 15: Project flow chart

3.4 Objectives and project plan

The background literature on ablation casting strongly suggests that there were several pieces of missing information critical to obtaining a comprehensive understanding of the HiPerMag process. This includes a model to predict casting grain size based on process parameters such as the jet activation delay time and also the prediction of the required jet parameters based on solidification and microstructural criteria. The various solidification criteria are listed below:

- limiting grain size variation by ±10 μm throughout the part;
- the majority of heat extraction takes place via the water jets;
- the sand mold should be of sufficient thickness for heat retention;
- gas and shrinkage porosity must be minimized.

Based on the solidification criteria, the following are the main objectives of the project:

- develop a viable water soluble sand binder system for the HiPerMag casting application;
- develop a sand mold geometry with an optimum thickness based on heat transfer criteria and processing conditions;
- quantify the solidification and jet parameters necessary to develop an empirical solidification model for a thin walled Al-alloy part.

The objectives of this project demand that the sand mold/binder system and solidification experiments be carried out with several independent parameters, as discussed below.

The required properties of the sand binder system developed for the HiPerMag casting application includes having an optimum green and dry strength, a gradual erosion rate under the action of the HiPerMag water jet and a binder with a relatively high water solubility. The sand mold thickness will be optimized based on heat transfer characteristics to obtain an optimum mold geometry. The optimized mold was used as an input to module II of project for studying the sand erosion rate as a function of jet momentum.

In order to properly understand the solidification of a thin walled, high aspect ratio castings, small scale thin walled (6 mm) plate casting trials were carried out. The objective of these experiments was to determine the effect of experimental parameters such as jet activation delay time and jet spacing on casting grain size, solidification front velocity and the surface integrity of the casting (examples are shown in Figure 16). Experimental constants included the liquid metal pouring temperature, and jet stand-off distance. Plates were cast with a single HiPerMag jet located near the edge of the plate. This was done based on results from conventional casting experiments in which it was observed that the edge cooled more quickly than the center due to the additional

surface available for conductive heat transfer. Hence, it was necessary to start cooling the part from the edges as they have a narrow solidification time window on account of the high cooling rate. In the current series of experiments, the movement of the solidification front was observed as a function of distance from the stagnation point of the water jet located near the edge. In order to maintain a single solid-liquid interface throughout the part and avoid regions of high shrinkage (which can lead to cracks as shown in Figure 17 [36]), it was necessary that the second jet should impinge on the part after the solidification front had reached the farthest point under its coverage, point Q in Figure 18. Also, microstructural analysis was carried out to determine the extent of grain refinement obtained by the single jet. This criterion in combination with the velocity of the solidification front was used to determine the spacing between the jets and their activation timing.

Figure 16: Plate with and without surface defects

Figure 17: Crack formation due to the meeting of two solidification fronts in the case of two HiPerMag jets (note: numbers on the plate show the regional pressures)

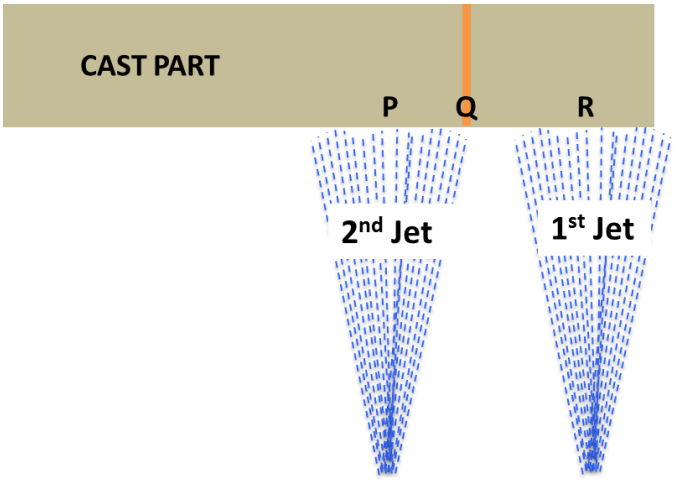

Figure 18: Location of solidification front (point Q) at the time the second jet impinges on the plate. R and P are stagnation points of 1st and 2nd jet respectively

Chapter 4: EXPERIMENTAL METHODOLOGY

This chapter is divided into five sections. In the first section, the details of the experimental setup are presented. In the second section, the procedures for mold fabrication and plate casting are described. The third and fourth sections present the experimental matrix and the scheme for microstructural analysis. Finally, in the last section, an analytical solution to the mold heat transfer problem is derived which determined the minimum insulating wall thickness for a conventional casting case.

4.1 Experimental set up

The experimental HiPerMag jet setup consisted of a centrifugal pump connected to a water tank. The pump was in turn connected to a series of nozzles via proportional solenoid valves and pressure transducers which controlled the jet flow via a standard controller. Proportional solenoid valves were placed at each branch of the piping from the manifold. The pressure transducers were placed before the manifold and at every branch of the hosing. The sand mold was placed inside a plexiglass chamber with nozzles below the mold, as shown in Figure 19. K type thermocouples were inserted into the sand mold as well in the casting as shown in Figure 20. The pressure of the water jet was initially high at 558.5 kPa (80 psi) to facilitate rapid sand removal and was then switched to a lower value of 172.4 kPa (25 psi) when directly cooling the part.

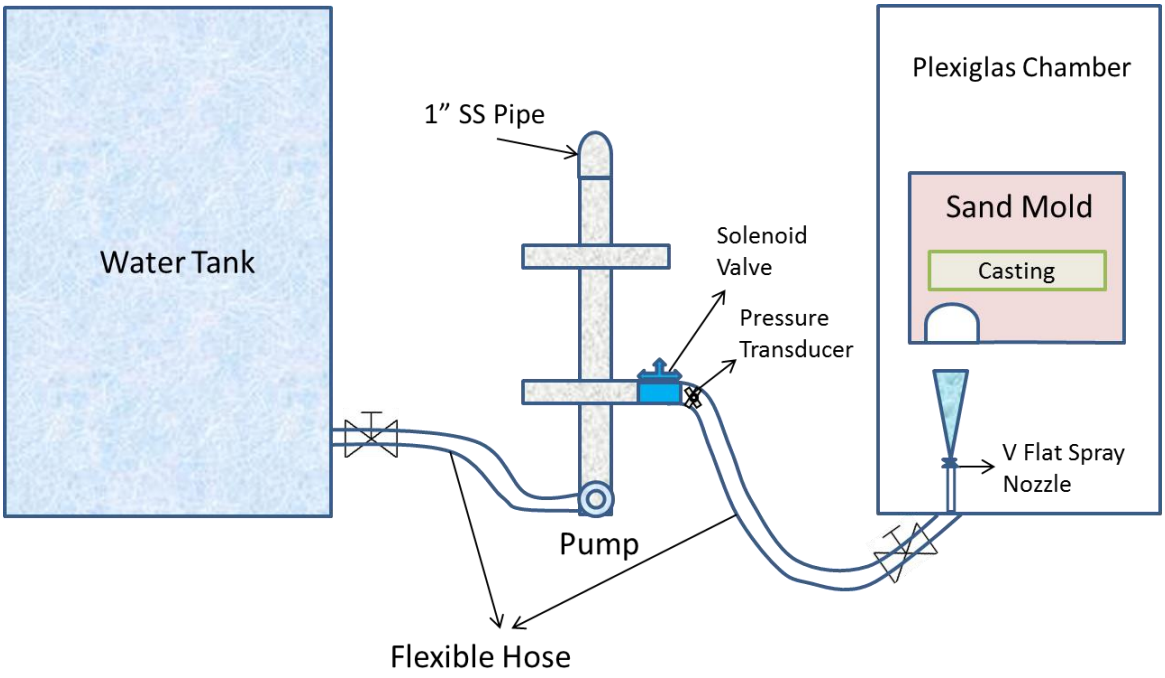

Figure 19: Experimental set up for the HiPerMag jet system

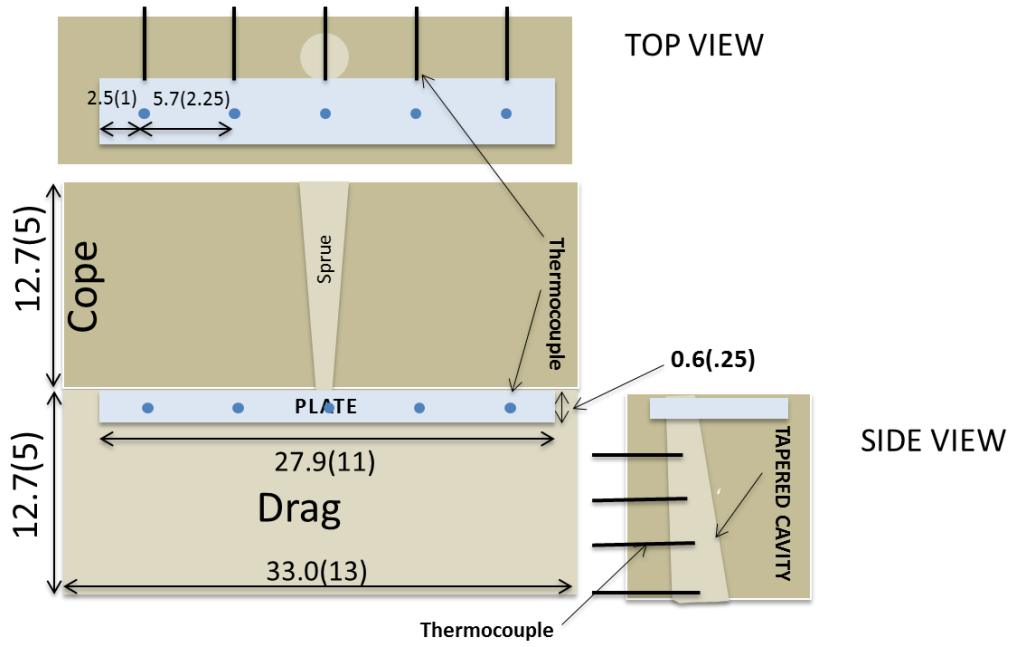

Figure 20: Schematic of mold showing K-type thermocouples inserted from side into the casting (all dimensions in cm with numbers in brackets showing dimensions in inches)

Flat "V" spray nozzles as shown in Figure 21, with a spray angle of 50° were used as they created an approximate 1:1 ratio between the standoff distance and spray coverage, where the standoff distance refers to the distance between the surface of the sand mold (the drag) and the nozzle. The long axis of the nozzle was parallel to the length of the plate (i.e. perpendicular to the solidification front). The jet was positioned such that the nozzle head was vertically below the edge thermocouple. The mold was de-molded from the bottom (i.e. the drag side of the mold, Figure 20), to prevent water accumulation on the casting and to enhance cooling of the part. A comprehensive listing of the hardware components used in the construction of the HiPerMag jet apparatus is provided in Table 3.

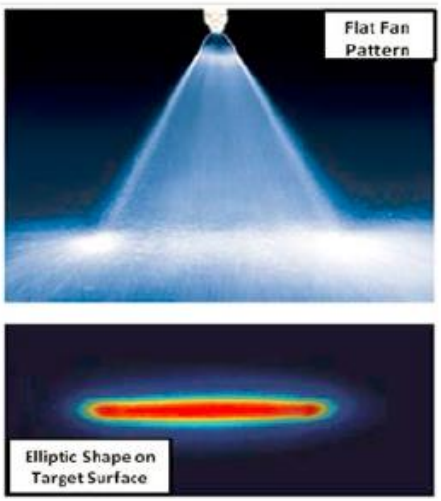

Figure 21: Flat V spray nozzle[37]

Table 3: Various components in the HiPerMag jet experimental apparatus

Equipment	Specification(s)	Manufacturer
Pump	2 HP Multi-Stage Centrifugal Pump	Gould Pumps
Data acquisition system	Max. Sampling Rate: 500 k⁄s	National Instruments
Rotameter	Max. Flow Rate: 5.5×10^{-4} $m^3⁄s$	Kobold
Thermocouple	K type, Range: -270 °C to 1372 °C, Error ± 1.1 °C or 0.4 %	Omega
Nozzle	Angle: 50°, Flat Fan-Shaped Spray Pattern	Bex Spray Nozzles
Solenoid Valve	Flow Range: 1.39×10^{-4} $m^3⁄s$ 3.53×10^{-3} $m^3⁄s$	Danfoss
Pressure Transducer	Pressure Range: 0 – 1035 kPa, Error: ± 2%	Omega
Computer	Prodesk, 4 GB RAM, 3.40 GHz Intel I3 Processor	HP
Mixer	6.62 L(7 Quarts)	Kitchenaid

The molds for the plate casting experiments were prepared at CanMaterials Laboratory, Hamilton using a mixture of 1.3 wt. % alphaset binder and AFS 75 silica sand.

The binder composition of 1.3 wt. % alphaset was chosen as it is commonly used [42] and was also recommended by the manufacturer. The molds were prepared with a slot used for filling water soluble binder mix as shown in Figure 22.

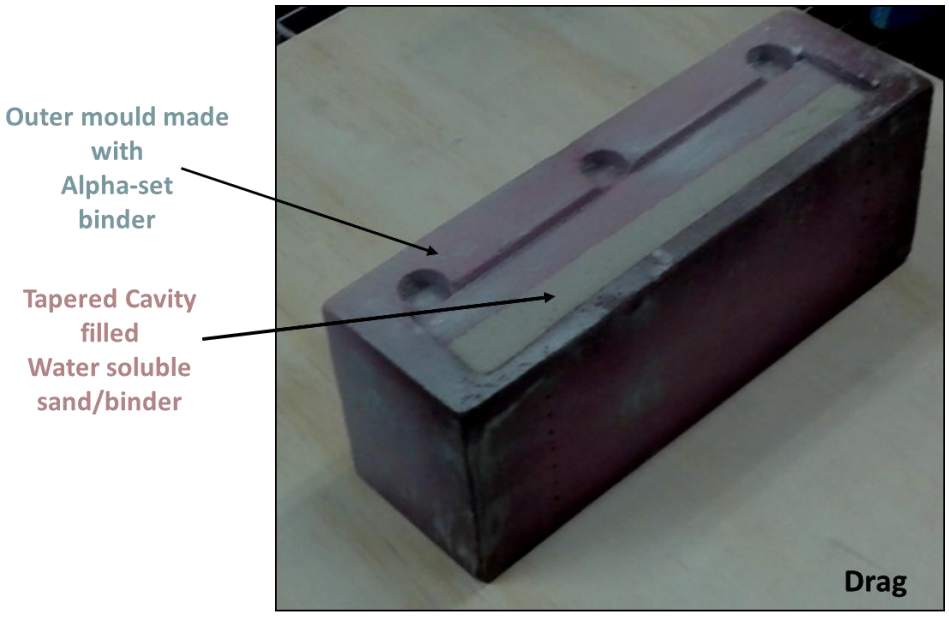

Figure 22: A composite mold

For plate casting experiments to determine the optimal HiPerMag jet spacing and timing, a master experimental melt of 22.67 kg (50 lbs.) was prepared in a graphite crucible, from which 500 g ingots were cast in small alumina crucibles for individual casting experiments.

The alloy was prepared using commercial purity Al ingots and Al-Cu, Al-Mg and Al-Cu-Zn-Mg-Fe and Al-Ti master alloys. The melt was periodically skimmed to remove the oxide layer, however, no melt degassing was done. The liquidus and the solidus temperatures of the alloy, as determined by PANDAT software, were 633 °C and 489 °C respectively. The target alloy composition is shown in Table 4.

Table 4: AA 7050 alloy composition [38]

Element	Weight %
Al	89.0
Cu	2.0
Mg	2.0
Zn	6.0
Ti	0.15

In later part of the study, it was realised that a more commonly used alloy such as AA 6061 with well reported values of grain size and mechanical properties as a function of cooling rate would be more suitable for use in the HiPerMag casting process as it would serve as a standard to which the experimental results could be compared. For this purpose, a second master experimental melt of AA 6061 alloy was prepared with the target composition shown in Table 5. The alloy was prepared using commercial purity Al ingots and Al-Cu, Al-Mg and Al-Si master alloys. The liquidus and the solidus temperatures of the alloy, as determined from the PANDAT software, were 652 °C and 582 °C respectively.

Table 5: AA 6061 alloy composition [38]

Element	Weight %
Al	98.2
Cu	0.19
Mg	1.01
Si	0.60

4.2 Experimental procedure

4.2.1 Fabrication and compression testing of water soluble sand mix

The fabrication and compression testing of the water soluble sand mix samples was carried out at CanMaterials Laboratory, Hamilton. The procedure for fabrication and testing of cylindrical test samples pictured in Figure 23 was as follows:

1. Dry AFS 75 silica sand was mixed with bentonite (6 wt. %), sodium dihydrogen phosphate (1.2 wt. %), borax (3 wt. %), plaster of Paris (3 wt. %) and water (3 wt. %) in a mixer for 10 minutes;
2. Standard 3-Ram compression test samples of 5.1 cm diameter and 5.1 cm height (Figure 23) were made by ramming the sand mixture into a specimen tube;
3. For the measurement of green compressive strength, the green samples were loaded and tested in an universal sand testing machine (as shown in Figure 24);
4. For evaluating dry compressive strength, the green samples were heated in an oven at 200 °C for 30 min to remove any moisture. The samples were removed from the furnace and allowed to cool to room temperature. The samples were then tested in the universal sand tester pictured in Figure 24.

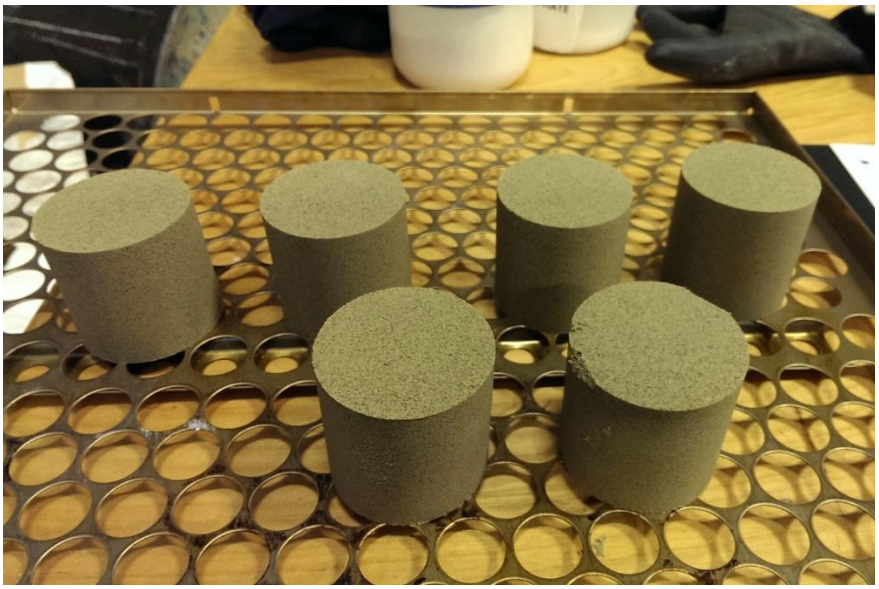

Figure 23: Water soluble sand mix compression test samples

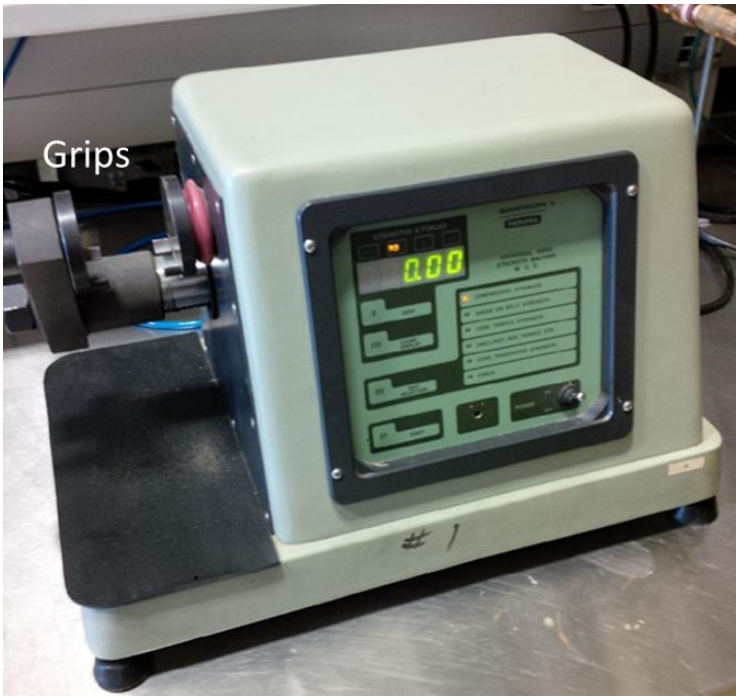

Figure 24: Universal sand testing machine showing grips for the compression test samples

4.2.2 Procedure for tensile testing and density measurement of alphaset bonded sand

The tensile testing and density measurement of the alphaset bonded sand were carried out at CanMaterials Laboratory, Hamilton. The experimental procedure for the same is described below:

1. Dry AFS 75 sand premixed with alphaset binder (1.3 wt. %) in a continuous sand mixer was collected and hand rammed into an AFS standard dog bone core box;
2. Ten minutes after packing the sand into the core box, the hardened mold samples were removed from the core box;
3. The samples were then tested in the universal sand testing machine with tensile grips (Figure 25) with time delays of 12, 30, 60 and 100 min measured after removal from the core box;
4. For measurement of the density of the alphaset bonded sand, premixed sand from the continuous sand mixer was collected and hand rammed into a rectangular pattern box of known volume. The hardened sand mold was removed after 10 min and massed on a balance. The density was calculated as the ratio of the mass to the volume.

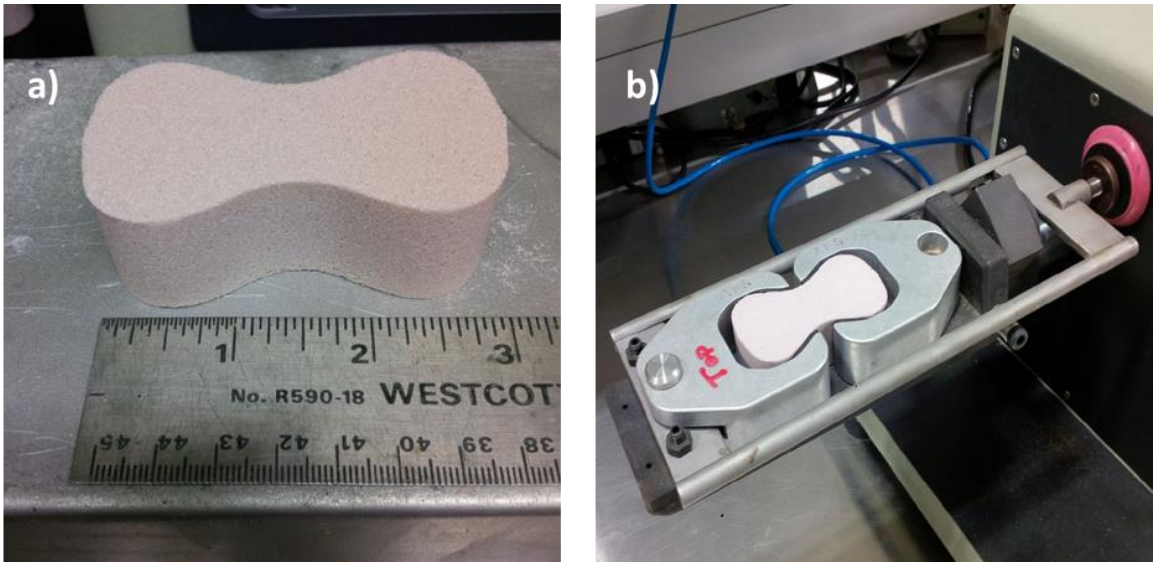

Figure 25: a) Dog-bone tensile sample for testing strength of alphaset bonded sand b) Sample held by tensile grip of the tester

4.2.3 Procedure for making the plate casting mold

The plate casting molds were made at CanMaterials Laboratory, Hamilton. The procedure for making the molds is described below:

1. The mold box was assembled over the match plate pattern which was coated with mold release;
2. Dry AFS 75 sand premixed with alphaset binder (1.3 wt. %) in a continuous sand mixer was collected;
3. A wedge was put over the match plate to provide a slot for filling in the water soluble binder/sand mixture;
4. The AFS 75 sand mixture was rammed around the wedge in the mold box;

5. After allowing the sand to harden for 10 minutes, the match plate was flipped and removed from the mold box;
6. The wedge was removed from the box;
7. The mold box was opened and the sand mold removed;
8. For making the cope, a sprue was placed in the groove on the match plate pattern and the above procedure was repeated.

4.2.4 Procedure for filling water-soluble sand-binder mix into the plate casting mold

The tapered slot in the mold was filled with the water soluble sand mix after which the mold was baked to cure the water soluble mix as per the procedure mentioned below:

1. All chemicals (bentonite (6 wt. %), sodium dihydrogen phosphate (1.2 wt. %), borax (3 wt. %), plaster of Paris (3 wt. %)) were mixed together with AFS 75 silica sand and water (3 wt. %) for 20 min in the mixer;
2. The plate pattern was inserted into its place in the mold and the mix was then rammed into the slot in the mold from opposite side;
3. The composite mold (Figure 22), was then baked in a furnace at 200°C for 2 hours;
4. The baked mold was allowed to cool to room temperature.

The mold was now ready for casting. It was placed such that the water soluble binder-sand slot was vertically aligned with the water jet. Thermocouples were inserted in the prescribed locations inside the mold cavity and also in the mold, as shown in Figure 26.

4.2.5 Plate casting procedure

After preparing the composite mold, the HiPerMag casting of the plate was carried out as per the procedure mentioned below:

1. A small 500 g alloy ingot prepared earlier was melted in a box furnace which was set at 760 °C;
2. A single HiPerMag jet was placed near the edge of the plate, as shown in Figure 26, initially to study the movement of the solidification interface;

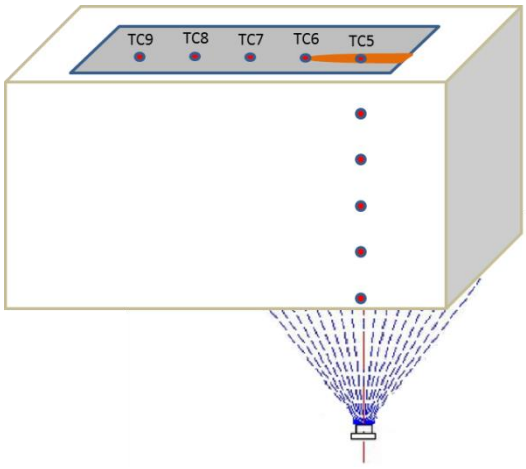

Figure 26: Jet location for the single jet case

3. After placing the thermocouples in the mold cavity and sand mold, they were connected to a data acquisition system with a sampling rate of 1 Hz. The water pump was switched on to establish flow in the system;
4. The sand mold was placed such that the HiPerMag nozzle head was vertically below TC5, as shown in Figure 27;

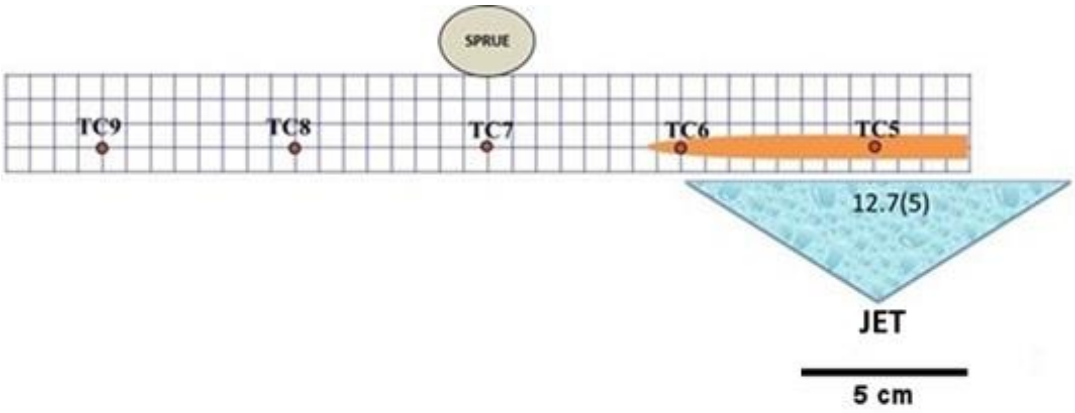

Figure 27: The jet and thermocouple locations (dimension shown is in cm with number shown in brackets in inches)

5. The metal was then poured into the mold at the previously established casting temperature of 730°C, measured by a hand held thermocouple. The water jet was started when the edge thermocouple TC9 (Figure 27) read a particular target temperature which was varied as per the experimental matrix (Table 6). The jet pressure was kept at 558.5 kPa (80 psi) for 4.7 sec then reduced to 172.3 kPa (25 psi). The stand-off distance (i.e. the distance between the drag surface and nozzle) was kept at 13.97 cm (5.5 in.);
6. After casting, the part was taken for microstructural analysis.

4.3 Experimental matrix

The experimental matrix for the study is shown in Table 6. The delay time (i.e. the time between the end of pouring to the start of jet HiPerMag) was varied based on five different TC9 temperatures of 600, 620, 625, 633 and 635 °C. In each case, the HiPerMag jet was activated when the thermocouple TC9 (Figure 27) showed this value of temperature.

Table 6: Experimental matrix for the jet HiPerMag study

Case No.	Jet start temperature at TC9 (°C)	Casting type
1	NA	conventional
2	600	HiPerMag
3	620	HiPerMag
4	625	HiPerMag
5	633	HiPerMag
6	635	HiPerMag

4.4 Microstructural analysis

The cast plates were cut as per the schematic shown in Figure 28, hot mounted and polished using standard metallographic procedures and etched for microstructural analysis. Conventional plate samples were etched using Keller's reagent (2.5 ml HNO_3,

1.5 ml HCl and 1.0 ml HF in 95 ml water), while for the HiPerMag cast plate samples, electrolytic etching using Barker's reagent (2.5 ml HBF_4 in 100 ml water) was carried out at 28.0 V for a time of 2 min per sample. Analysis of the sample's microstructure was conducted using a Nikon optical microscope and ImageJ software. Sample grain size was determined using the ASTM linear intercept method [39].

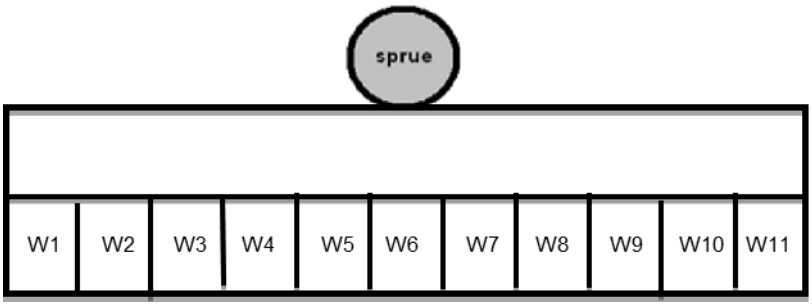

Figure 28: Microstructure locations

4.5 Heat transfer through the walls of a conventional sand casting

As the liquid metal is poured into a sand mold which is at ambient temperature, the metal solidification takes place by conduction of heat from the metal to the mold. As a result of this, a thermal gradient develops across the sand mold which depends on the thermal conductivity and thermal diffusivity of the sand (which is very low for commonly used silica foundry sands). As would be expected, the thermal gradient is higher near the mold cavity and decreases with increasing the mold thickness to a point at which it becomes negligible. However, as the diffusion of heat is time dependent, a point inside the sand mold that shows no temperature rise at small times may start showing a rise in

temperature as time progresses. The mold thickness required to achieve a condition where the thermal gradient is negligible even after long times after mold filling is complete would be referred to as the "critical mold thickness" in the following text. In order to determine the critical mold thickness, an analytical solution was derived for studying the temperature distribution in a sand mold during the solidification of a conventional casting. The critical mold thickness derived was then used as a reference point for designing a mold for the HiPerMag casting experiments since the casting solidifies in a conventional way during the initial stage of the HiPerMag casting process (i.e. before the water jet impinges on the part). Determination of this thickness ensures that the liquid metal is sufficiently insulated until the time it is contacted by the water jet. For the purposes of this analysis, the mold was assumed to be semi-infinite and the casting relatively thin such that the Biot (Bi) number was quite low (i.e. $Bi \leq 0.1$). This assumption resulted in there being a negligible temperature gradient between the liquid metal and solidified metal, as pictured in Figure 29. Thus, the major resistance to heat flow was the mold itself [40].

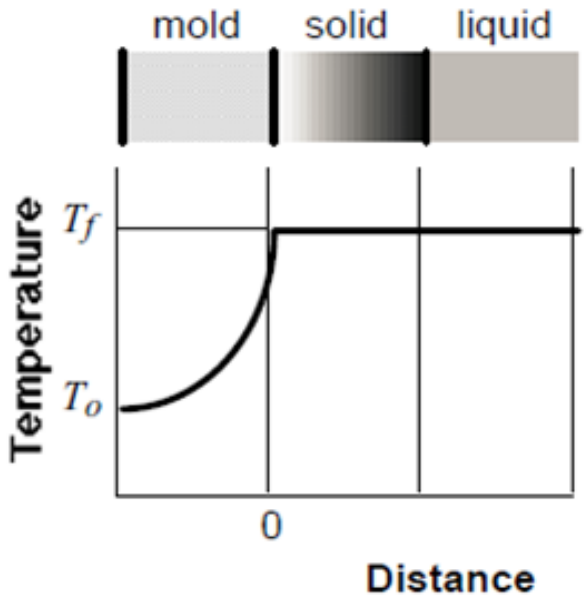

Figure 29: Temperature distribution in a sand mold showing the thermal resistance in sand mold and negligible thermal resistance at the solid-liquid interface [41]

For the case of a thin walled casting solidifying in a semi-infinite mold, the evolution of the thermal gradient across the sand mold can be approximated by 1D transient heat flow without a source or sink term, given by:

$$\frac{\partial T}{\partial t} = \alpha \frac{\partial^2 T}{\partial x^2} \tag{1}$$

where T is the temperature at the interface, t is time, $\alpha = \frac{k}{\rho C_p}$ is the mold material thermal diffusivity, where k, ρ and C_p are the mold thermal conductivity, density and constant pressure heat capacity, respectively, and x the length dimension for heat transfer. The solution to this equation takes the form [41]:

$$T = C_1 + C_2 erf(u) \quad where \quad u = \frac{x}{\sqrt{2\alpha t}} \tag{2}$$

If $x = 0$ is chosen to be at the solid/mold interface (Figure 29), the assumption of a semi-infinite mold results in the thermal boundary conditions (BC) being given by:

BC1: $T = T_0 \quad at \quad x = -\infty$
BC2: $T = T_f \quad at \quad x = 0$

where T_f is the fusion temperature of the metal, and T_0 is the ambient temperature. The use of BC1 in equation (3) yields the result:

$$T_0 = C_1 + C_2 erf(-\infty) = C_1 - C_2 erf(\infty) = C_1 - C_2 \tag{3}$$

and BC2 yields:

$$T_f = C_1 + C_2 erf(0) = C_1 \tag{4}$$

which yields the general result for the temperature in the mold as a function of position (x) and time (t) [41]:

$$T = T_f + \left(T_0 - T_f\right) erf\left(\frac{x}{\sqrt{2\alpha t}}\right) \tag{5}$$

Based on the physical properties of the mold material shown in Table 8, a melt fusion temperature of 720 °C and an ambient temperature of 25 °C, the mold temperature as a function of mold wall thickness and time was determined. The mold temperature as a function of time for various positions from the mold metal interface (1, 5, 10, 50 and 100 mm) is shown in Figure 30.

It is evident from the plots that there is no change in the temperature inside the mold at thicknesses beyond 100 mm, even at very large times. Hence, a mold thickness of 100 mm (4 in.) was deemed sufficient to provide insulation for the hot metal for the initial part of the HiPerMag casting process in which the metal cooled in a conventional way.

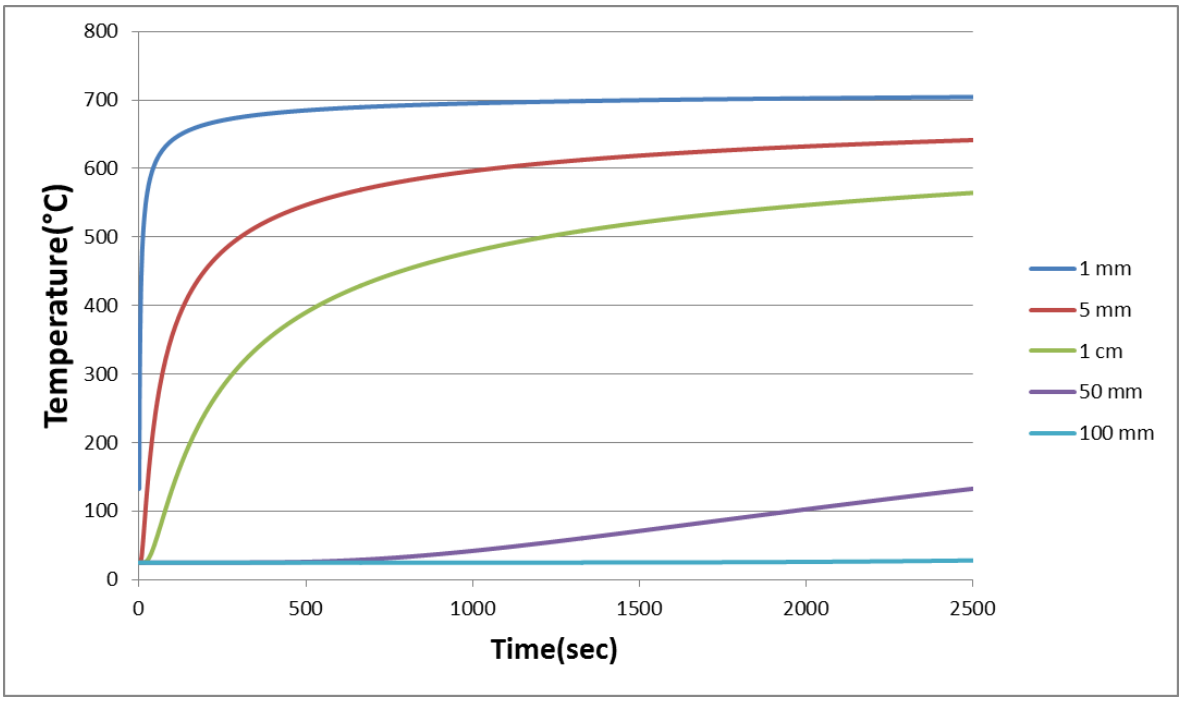

Figure 30: Temperature vs. time plot for various locations in the sand mold

Chapter 5: RESULTS AND DISCUSSION

5.1 Sand binder system:

The information regarding the composition of the water soluble binder was obtained from the patent of Goetz et al. [3]. An addition of 6.0 wt. % bentonite to the original composition was done to improve the de-molding characteristics of the sand binder mix–i.e. to make the de-molding gradual. In addition, 3.0 wt. % plaster of Paris was added to improve the green strength.

The green and dry strengths of the water soluble binder mix were evaluated per the procedure mentioned in section 4.2.1. The results of these tests are shown in Table 7.

Table 7: Green and dry strength of sand binder mix

Test No.	With POP	
	Green Strength (kPa)	Dry Strength (kPa)
1	157.2	4014.1
2	157.2	3876.2
3	162.7	3359.1
4	162.2	3847.3
5	158.6	4029.3
Average	159.6 ± 3.1	3825.2 ± 313.7

POP: Plaster of Paris

Similarly, tensile tests were carried out for alphaset binder system per procedure outlined in section 4.2.2 to study the effect of time after strip on the strength of the mold. In this case, strip time is the time after which the mold is removed from pattern

after the packing of sand into the mold. The tests were carried out at two most commonly used [42] binder levels of 1.3 wt. % and 1.5 wt. %. For the current study, a strip time of 10 minutes was used as this is most commonly used in commercial foundries [42]. These results are shown in Figure 31.

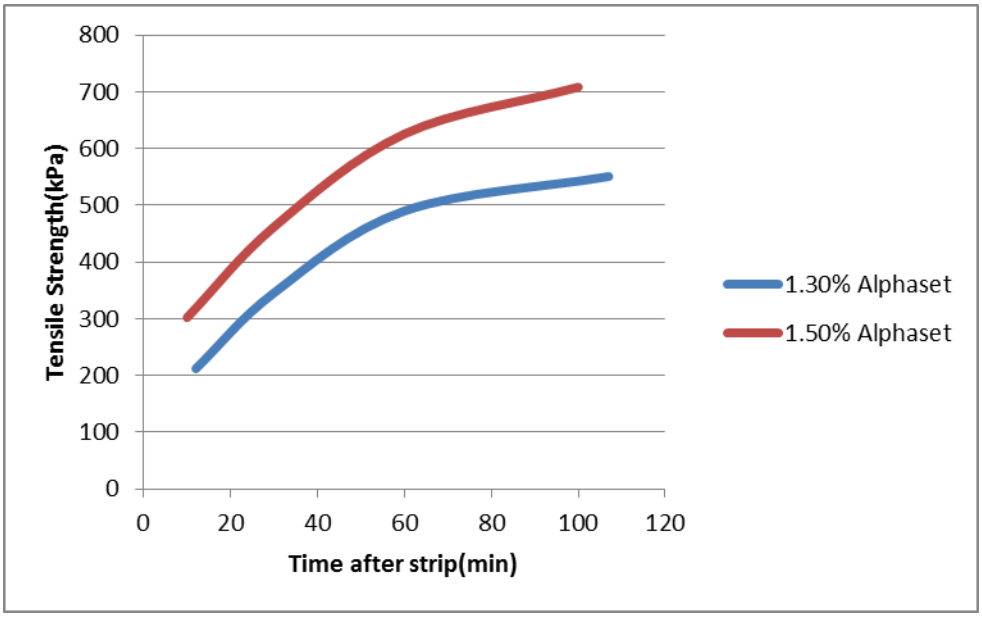

Figure 31: Tensile strength of the alphaset mold with time

It can be seen from Figure 31 that the mold strength increased with time after strip for both of the binder levels investigated. It can also be seen that the tensile strength increased when increasing the binder content from 1.3 to 1.5 wt. %.

5.2 Sand mold thickness determination

5.2.1 Sand mold thickness determination from the heat transfer model

A model was developed to study heat loss from the solidifying plate and find the minimum mold wall thickness sufficient to provide insulation for the solidifying metal. The heat flux in the plate's thickness direction (i.e. the x-direction, shown in Figure 32) was assumed to be the maximum due to its high specific surface area. The heat flux in the other two directions was neglected due to this assumption. Heat transfer in the mold occurred by three modes as shown in Figure 32.

Equation 8 for the total heat flux through the cope was derived based on fundamental heat transfer principles (i.e. heat flux equals the ratio of the temperature difference across the body to the total thermal resistance of the body). The thermal resistances and other parameters used in Equation 8 are defined below:

$L_p \equiv$ length of the plate = 27.9 cm

$W_p \equiv$ width of the plate = 5.1 cm

$h_g \equiv$ total heat transfer coefficient in the air gap ($h_g = h_{convection,air\ gap} + h_{radiation,air\ gap} + h_{conduction,air\ gap}$, but, $h_{radiation,air\ gap} << h_{convection,air\ gap}$ [43],[44] and $h_{conduction,air\ gap} << h_{convection,air\ gap}$, as k_{air} is low i.e. 0.024 [45] meaning that $h_g \approx h_{convection,air\ gap}$) = 420 W/m^2.K [48])

$k \equiv$ mold thermal conductivity = 0.45 W/m.K [47]

$T_\infty \equiv$ temperature of the surroundings = 25°C

$T_1 \equiv$ initial melt temperature = 720°C

$x \equiv$ cope thickness

$L \equiv$ length of the mold = 33.0 cm

$W \equiv$ width of the mold = 10.2 cm

$H \equiv$ heat transfer coefficient between the mold and the surrounding air = 12 $W/m^2.K$ [49]

$Q \equiv$ total heat flux

$R_1 \equiv$ convective resistance between the plate and the air gap ($1/h_g A_p$), where A_p is the surface area of the plate in the x direction

$R_2 \equiv$ conductive resistance through the mold (x/kA_p)

$R_3 \equiv$ convective resistance between the mold and the surrounding air ($1/hA_m$), where A_m is the outer surface area of the cope

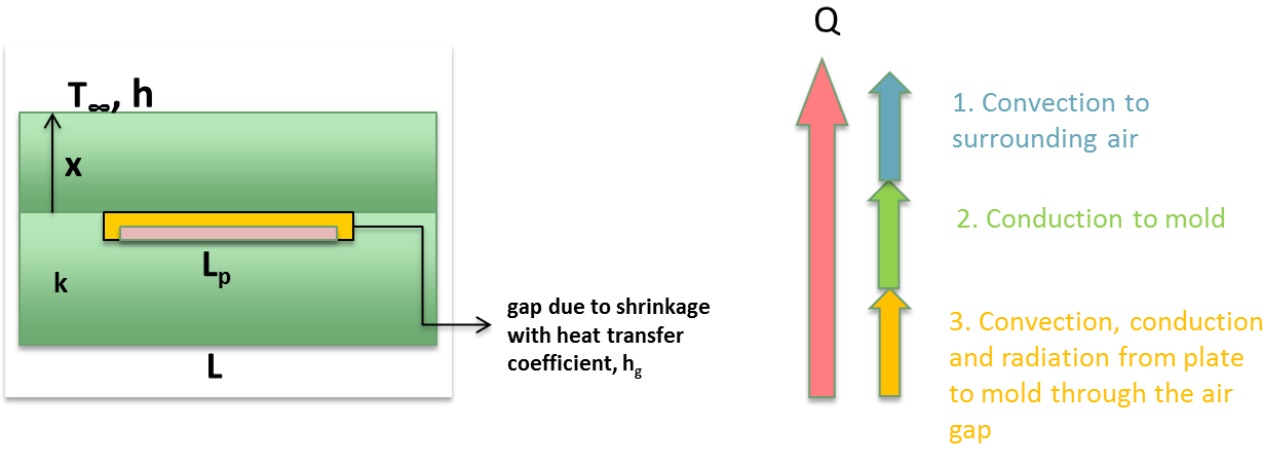

Figure 32: Modes of heat transfer in the experimental sand mold

$$Q = \frac{T_1 - T_\infty}{R_1 + R_2 + R_3} = \frac{T_1 - T_\infty}{R_1 + R_2 + R_3} = \frac{T_1 - T_\infty}{\frac{1}{h_p L_p W_p} + \frac{x}{k L_p W_p} + \frac{1}{h(LW + 2Lx + 2Wx)}} \quad (6)[46]$$

From Equation 8, a plot of Q vs. x was obtained using values of h, k and h_g from the literature (Table 8) as shown in Figure 33. From this plot it can be seen that the heat flux decreased asymptotically from a peak value of about 271 J/s at x=0 cm to about 29.5 J/s at x=12.9 cm. Hence, a mold with a cope of thickness 12.9 cm would lose heat at a rate of 29.5 J/s or about 10 % of the global heat loss of 271 J/s in the case where the cope thickness was kept at approximately 0 cm. Further, due to the asymptotic nature of the curve, an increase in the cope thickness to from approximately 12.9 cm to approximately 20 cm reduced the flux loss further by only 4 %. Therefore, a cope thickness of 12.9 cm was considered to be the critical thickness.

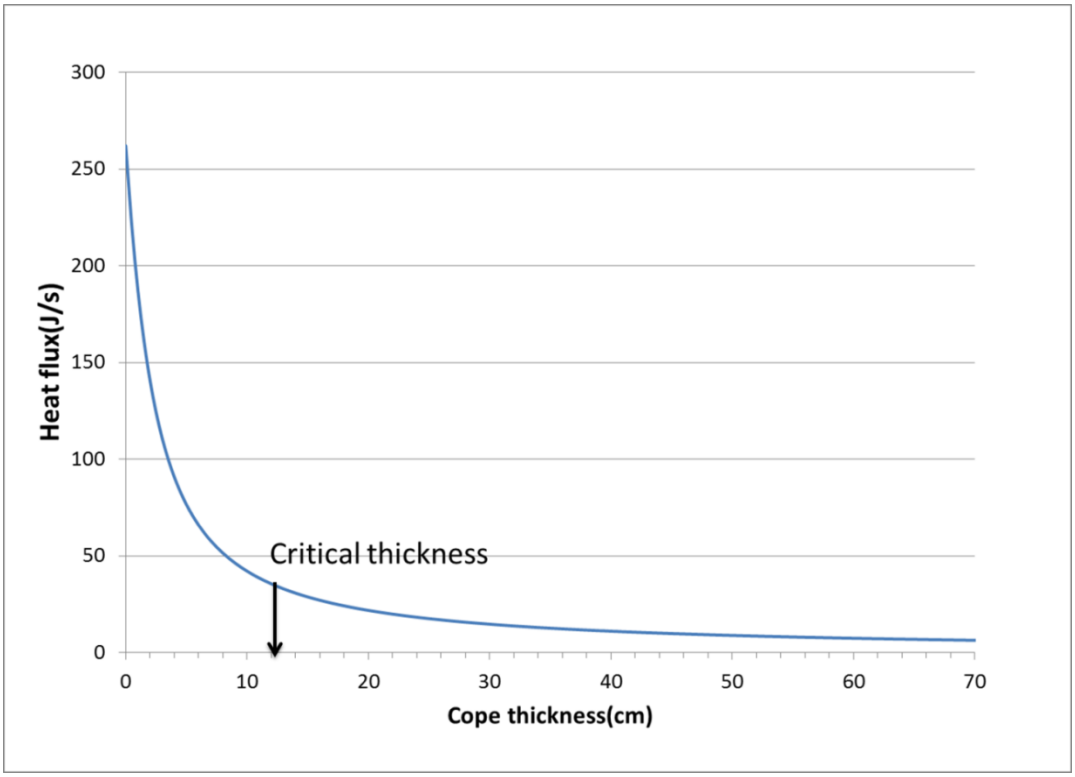

Figure 33: Determination of critical cope thickness

Based on above analysis, it was concluded that a cope thickness of 12.9 cm significantly reduced (by about 90%) the heat losses from a conventionally cast plate and, therefore, could be used to design a mold for the HiPerMag casting process which requires a sufficiently thick mold to keep the metal hot during the initial stage of the process. A mold with such a thickness ensures that the heat is extracted primarily by the water jets (instead of being lost by conduction through the mold) and also allows any entrapped gases to escape while the metal is hot, thereby minimizing gas porosity.

Table 8: Values for h_g, h and k from literature

Source	h_g ($W/m^2.K$)	k (W/m.K)	h ($W/m^2.K$)
[47]		0.45	
[48]	420		
[49]			12

5.2.2 Sand mold thickness determination from plate casting experiments

As the flow of heat is time dependent, it is understood that an arbitrary point inside the mold will start showing a rise in temperature after a certain time delay measured from the time when mold filling is completed. However, in the HiPerMag casting process, it is possible that the casting may be quenched before thermal diffusion causes any significant rise in temperature of the mold at that arbitrary point. A series of plate casting experiments were carried out to determine the minimum distance from the mold cavity at which such a transition would occur. The experiments were carried out with a cope thickness of 12.7 cm (5 in.)–i.e. close to that determined from the heat transfer model. The temperatures at various locations in the cope were measured using K type thermocouples–having error of ± 1.1 °C, during the HiPerMag casting process to

determine the critical cope thickness beyond which there was not a significant change in temperature for a defined period.

A conventional casting (i.e. without any water quenching) experiment was carried with thermocouples embedded in the casting as well as in the mold. One row of thermocouples was inserted in the mold at the distances from the plate shown in Table 9. A total of three thermocouples were inserted into the cast plate as shown in Figure 34. Figure 35 shows the thermal data obtained. It was found that it took approximately 52 s for the thermocouple located at 1.94 cm from the plate to show any significant rise in temperature after filling of the mold was completed.

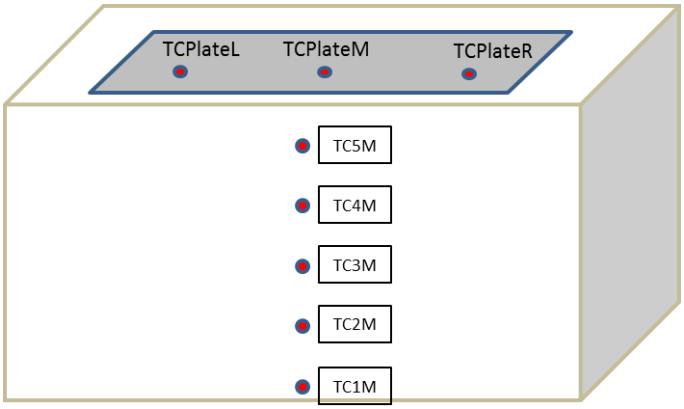

Figure 34: Thermocouple locations for conventionally cast plate

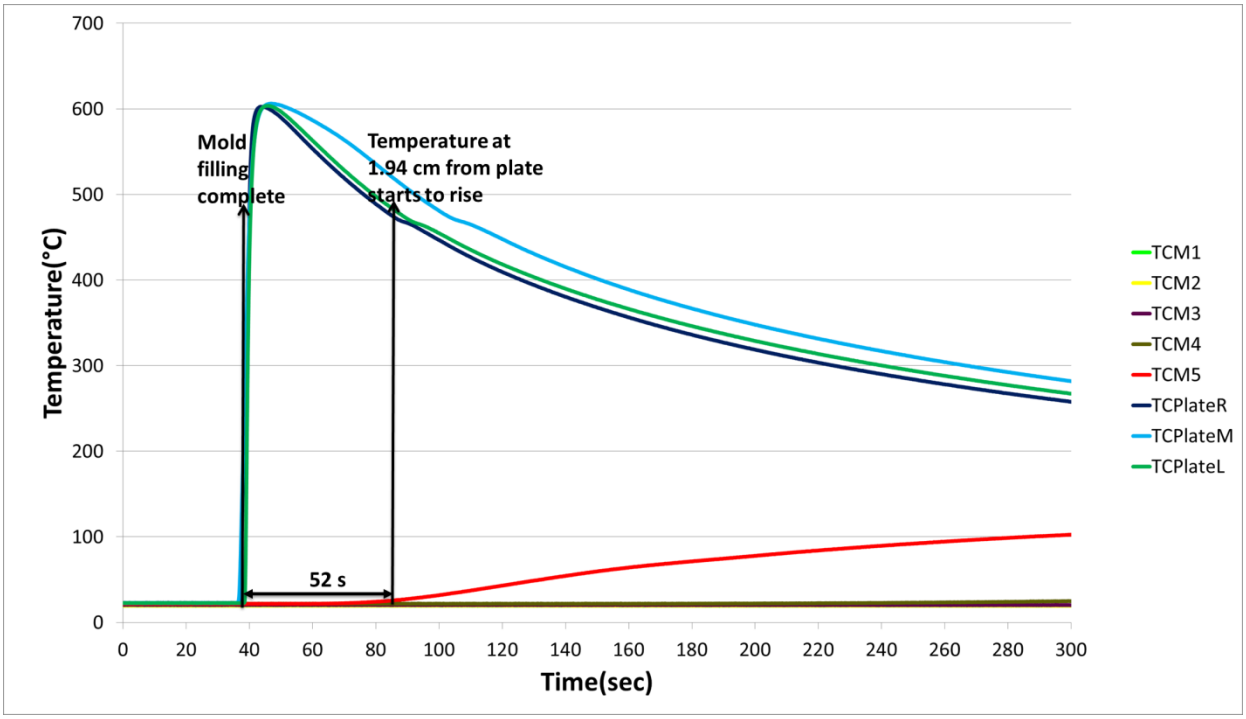

Figure 35: Temperature time plot showing for conventional casting (without water jets)

Table 9: In-sand thermocouple locations for conventional casting and three jets cooled casting

S. No.	Thermocouple	Distance from plate (cm)
1	TC1M	12.1
2	TC2M	9.56
3	TC3M	7.02
4	TC4M	4.48
5	TC5M	1.94

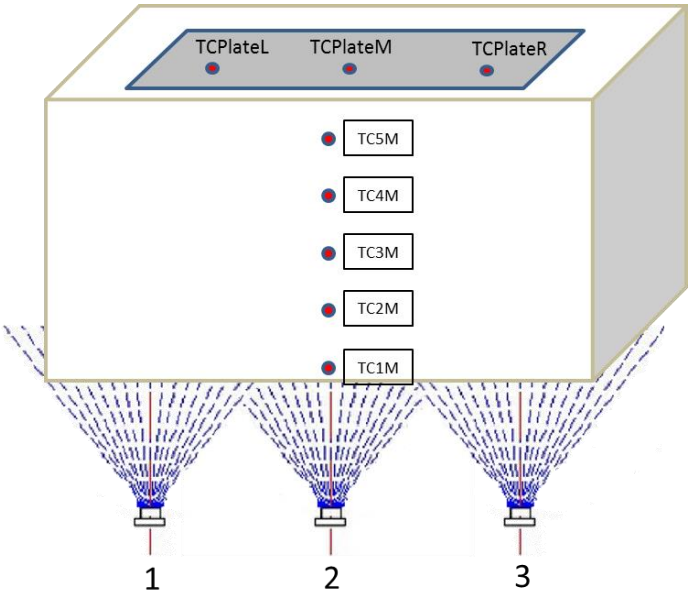

Figure 36: Thermocouple locations for case with three water HiPerMag jets

A similar experiment was conducted to determine the total process time with cooling provided by three water jets, where the thermocouple locations were kept the same as in the earlier experiment (see Table 9). A schematic of this set up is shown in Figure 36. For this test jets 1 and 3 were started immediately after pouring with a jet pressure of 551.5 kPa (i.e. a jet momentum of 5.6 kg.m/s) and were maintained at this pressure for 3 s after which the pressure was reduced to 103.4 kPa (i.e. a jet momentum of 0.933 kg.m/s). Jet no. 2 was started 2 s after the start of jets 1 & 3, with a starting pressure of 551.5 kPa which was maintained for 3 s after which it was reduced to 103.4 kPa. The spacing between the water jets was kept at 11.4 cm (4.5 in). The thermal data plots obtained from the thermocouples in the sand mold and in the plate are shown in Figure 37 and Figure 38. The time for the start of sand removal was calculated based on the blip in the thermal data resulting from the water jet striking the bottom-most

thermocouple (TC1M in Figure 36). The quench time was determined from the in cast thermocouple (TCPlateM in Figure 36) which was vertically above the in sand thermocouples. The middle row of thermocouples was chosen for timing analysis due to their proximity to the sprue as this is the location of maximum heat retention; hence, the cope thickness obtained would be the minimum.

It was found that in this case, there was a 32 s delay from the time when mold filling was completed to the time part was completely quenched as shown in Figure 38.

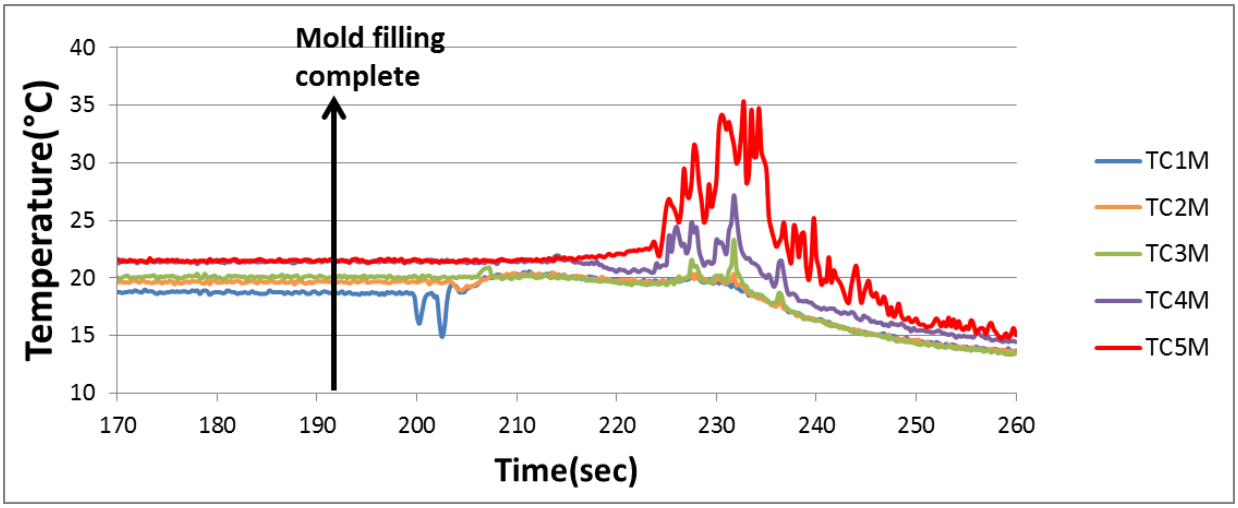

Figure 37: Temperature distribution at various thermocouple locations in sand for 3 jets case

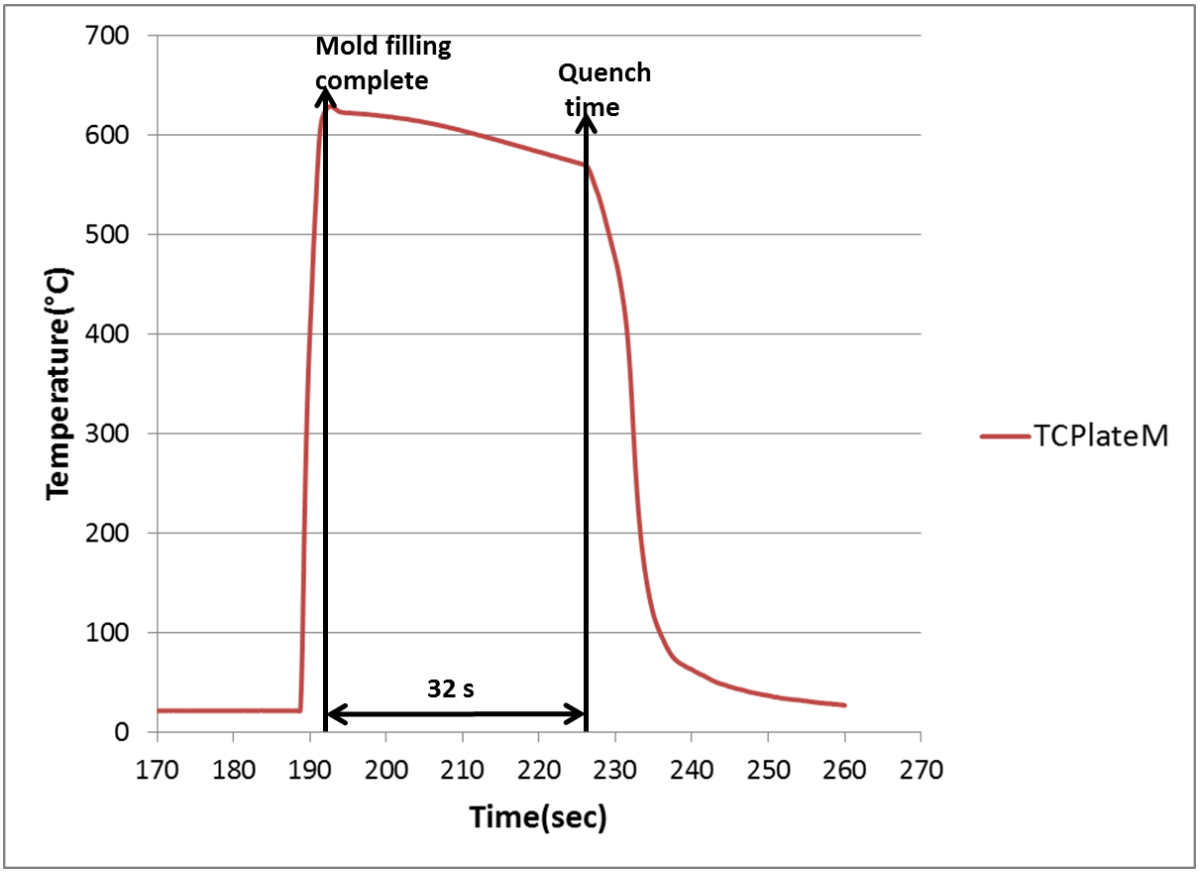

Figure 38: Mold filling time and quench time for test case with 3 jets

From these experiments, it was concluded that, since the duration of the initial stage of the HiPerMag casting process in which then molten metal cools in a conventional way was less than the time it took for the temperature to start rising at a distance of 1.94 cm from the plate (TC5M in Figure 35), found from the conventional casting experiment, a cope thickness of 1.94 cm was considered sufficient to provide the necessary insulation during the HiPerMag casting process. This was confirmed temperature measurements in the sand mold during the HiPerMag casting, where the thermocouple TC5M (Figure 37)

which was 1.94 cm from the plate, showed a temperature rise 34 s after mold filling was completed and recorded a peak temperature of 35°C.

However, a mold of this thickness may not be strong enough to handle, thereby precluding its use. Hence, in the following section, a minimum cope thickness based on strength will be determined.

5.2.3 Calculation of minimum thickness of sand mold based on strength

The minimum thickness of the cope based on strength considerations was calculated assuming it to be a beam subjected to a uniformly distributed load and fixed at both ends in case 1 (Figure 39) and a cantilever beam under uniform distributed loading in case 2 (Figure 40). The tensile strength and the density of the alphaset bonded sand were determined per the procedure discussed in section 4.2.2.

Case 1:

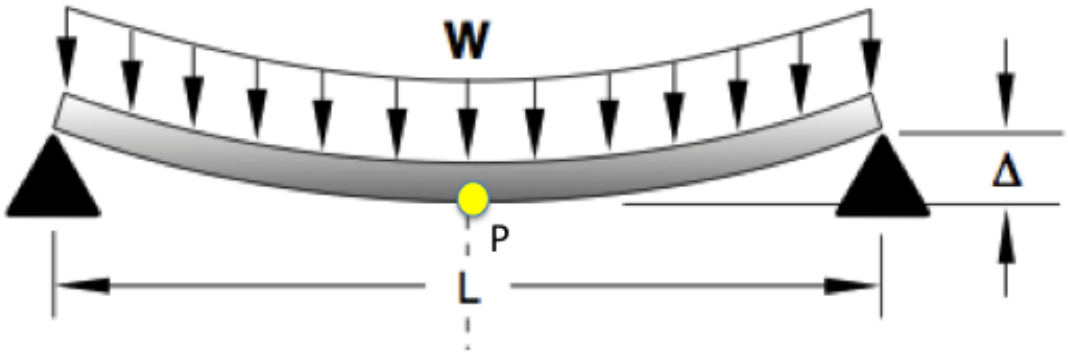

Figure 39: Beam under uniform loading fixed at both ends

The following parameters were used in the strength calculations for case 1 shown in Figure 39.

- $\rho \equiv$ mold density = 1681 kg/m^3;
- beam dimensions (assuming height of H) = 33.0 x 10.2 x H cm^3 or 13 x 4 x H in^3;
- the beam failure stress at point P is given by $\sigma_F = WL^2/8Z$ where $Z = bH^2/6$, where b= beam width and H = beam height and $W = \rho Vg/L$ = load per unit length where V is the beam volume and g is the acceleration due to gravity [50], [51];
- $\sigma_{TS} \equiv$ mold tensile strength (10 min after strip) = 344738 Pa (Figure 31).

Using the criterion that:

$$\sigma_{TS} \geq \frac{WL^2}{8Z} \tag{9}$$

for the cope dimensions such that it can meet the mechanical requirements and substituting the above values in Equation 9, it was determined H ≥ 0.40 cm.

Case 2:

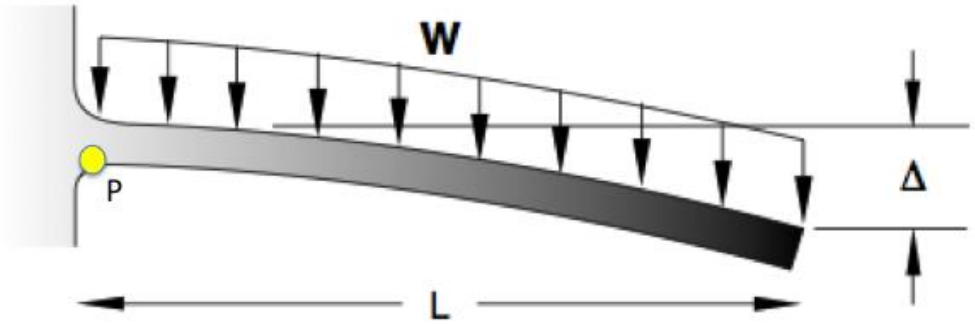

Figure 40: Cantilever beam under uniform loading

In this case (Figure 40), the beam failure stress at point P is given by $\sigma_F = WL^2/2Z$, where all terms are defined as above. Thus, the criterion for the minimum cope thickness is given by:

$$\sigma_{TS} \geq \frac{WL^2}{2Z} \tag{10}$$

From which the design criterion of H ≥ 1.60 cm was derived.

Based on the results of this case, the minimum sand mold thickness was set at 1.60 cm for the plate casting mold for it to not fail under its own weight.

5.3 Determination of jet timing and spacing

In order to cast a long part, multiple jets with precisely controlled activation timings and spacing to match the movement of the solid-liquid interface are needed. In order to

determine these process parameters, small scale plate casting experiments were carried out using the experimental setup and methodology explained in Chapter 4 (sections 4.1 and 4.2).

A schematic of the locations of the thermocouples and HiPerMag jet is illustrated in Figure 41 and details concerning the thermocouple locations are provided in Table 10.

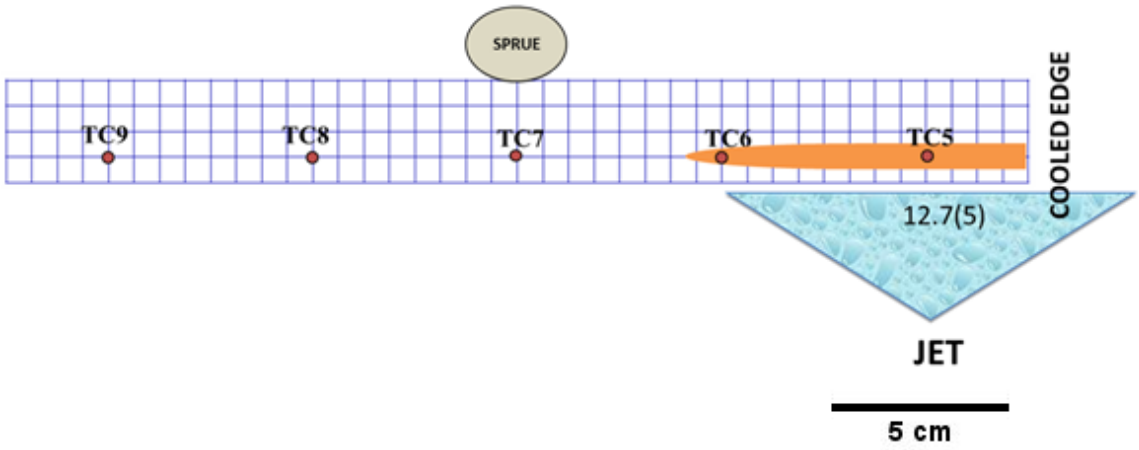

Figure 41: Jet and thermocouple locations (elliptical shaded area represents the jet impact region, dimension shown is in cm with number shown in brackets in inches)

Table 10: Distance of thermocouples from the cooled edge (Figure 41)

Thermocouple	Distance from the cooled edge cm(in)
TC5	2.54(1.0)
TC6	8.25(3.25)
TC7	13.97(5.5)
TC8	19.68(7.75)
TC9	25.4(10.0)

5.3.1 Thermal data analysis and HiPerMag jet activation delay

Figure 42 shows the temperature-time curve obtained for the jet HiPerMag process as a function of thermocouple location for the case of the HiPerMag jet being activated at 620 °C. It can be seen from Figure 42 that as the metal was being poured the temperature started to rise until a peak temperature was reached when the mold was filled. The thermocouples near the sprue (TC6, TC7 and TC8) recorded temperature above the liquidus (e.g. point A, Figure 42) while thermocouples on the plate edges (TC5 and TC9) remained below the liquidus. After mold was filled, the HiPerMag jet was activated when the thermocouple located on the edge TC9 read a defined value of the target temperature (i.e. 620°C for the data in Figure 42). This temperature will be referred to as the "jet starting temperature" hereafter. As the sand was gradually removed by the water jet the casting solidified in a conventional way as shown by the low slope value of the curve A-B (Figure 42). After all the sand was removed, the water jet impinged on the solidifying metal, and after some delay, a sharp drop in temperature occurred (e.g. point B for TC5, Figure 42) as the plate was directly quenched. The various thermocouples along the length of the plate registered this sharp decrease in temperature with a delay due to thermal diffusion through the plate.

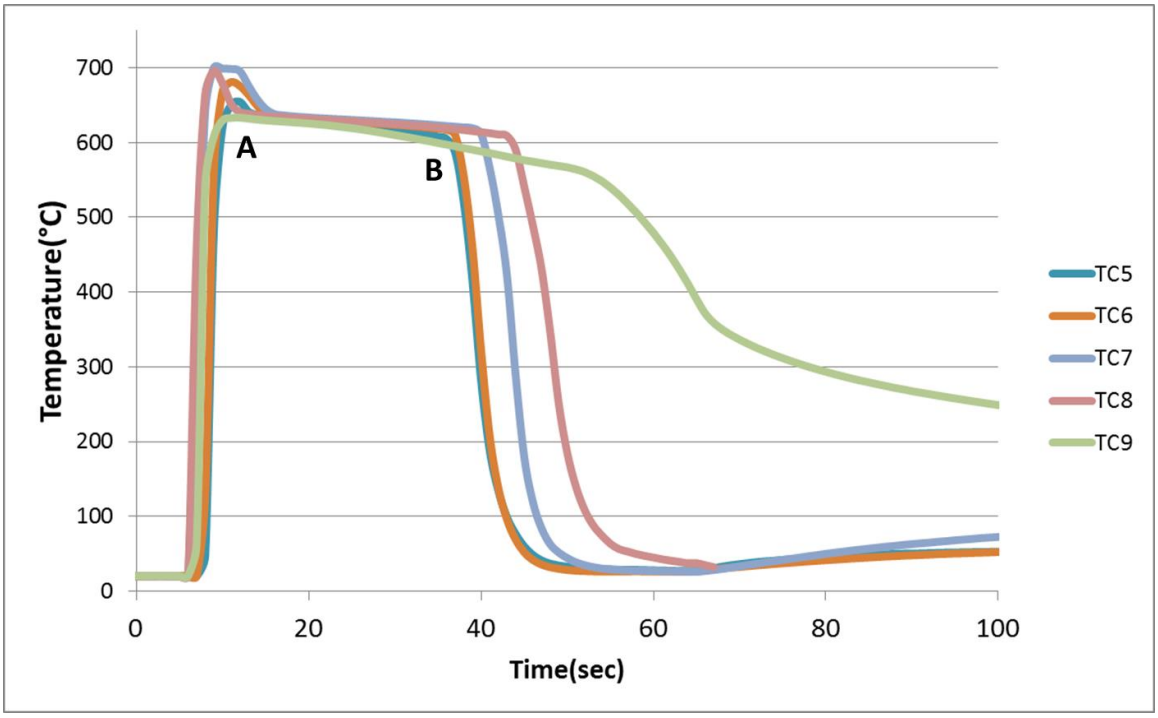

Figure 42: Time-temperature curves for HiPerMag jet activation at 620°C

From the thermal data in Figure 42, it can be seen that thermocouples TC5 and TC6 which were under the water jet impingement zone (Figure 41), had insignificantly different time-temperature profiles. Figure 43 shows a schematic of how the delay times due to the action of the water jet between the various zones of the casting were determined. For example, the delay time t1 is defined as the time between the onset of rapid cooling for TC5 and TC7, as shown in Figure 43. In this case, an additional delay of t2 seconds is defined as the time required for the solidification front to reach at TC7 (i.e. time at which eutectic solidification occurs at TC7, Figure 43).Hence time t1+t2 defines

the total delay time for the solidification front to reach TC7 from the start of quenching at TC5 (point B, Figure 42).

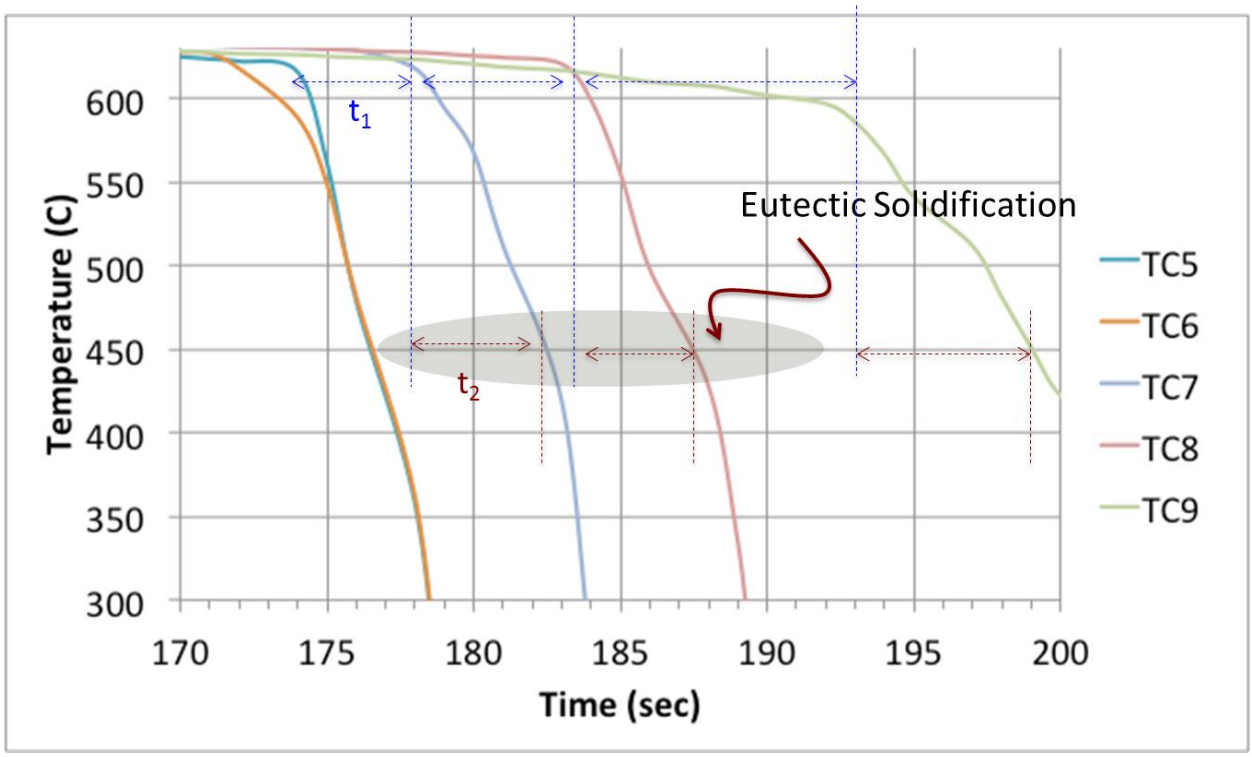

Figure 43: Delay time t1 and t2 determined from the temperature-time profiles of Figure 42

The delay times were plotted against the distance from the cooled edge for various impingement temperatures (measured with respect to thermocouple TC5) and a regression fit to the curve was determined. It was found that a logarithmic trendline fitted the data points with an r^2 value of approximately 0.9. Hence, the data was plotted as Ln of delay time vs. distance as shown in Figure 44.

It was found that the delay time did not vary significantly with the impingement temperatures explored. Since the initial solid fraction at the impingement time depends on the impingement temperature, it can be concluded that for a thin walled casting the initial solid fraction at the time of impingement had a negligible effect on the velocity of the solidification front. Also shown in Figure 45 is the regression fit to the data points with a 95 % confidence interval.

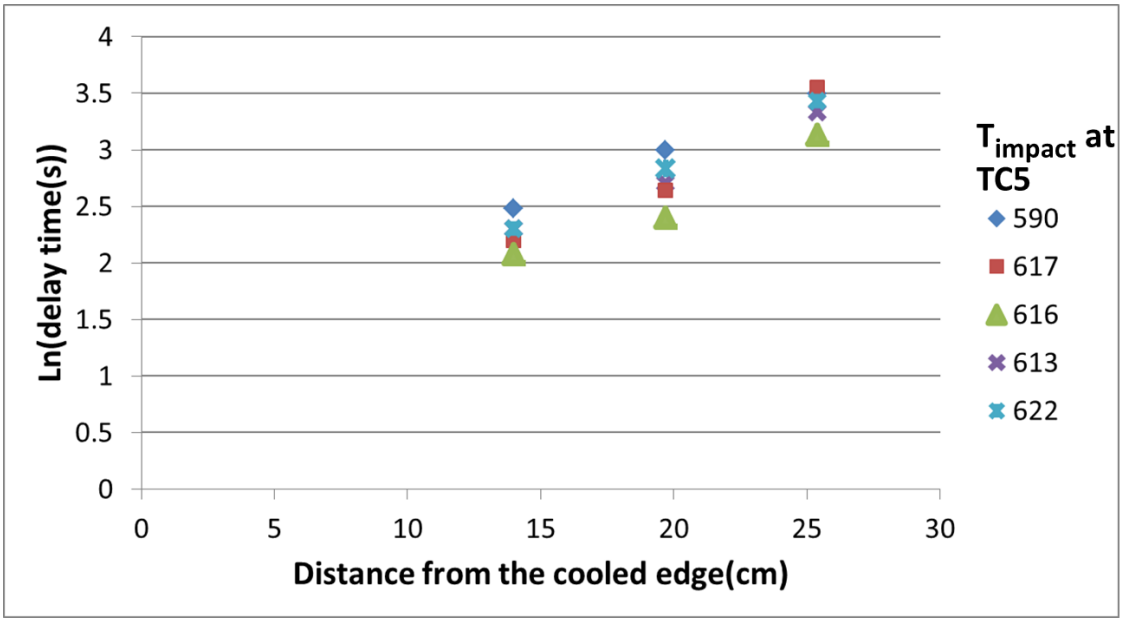

Figure 44: Delay time (t1+t2) versus distance from the cooled edge for various impingement start temperatures as measured at TC5

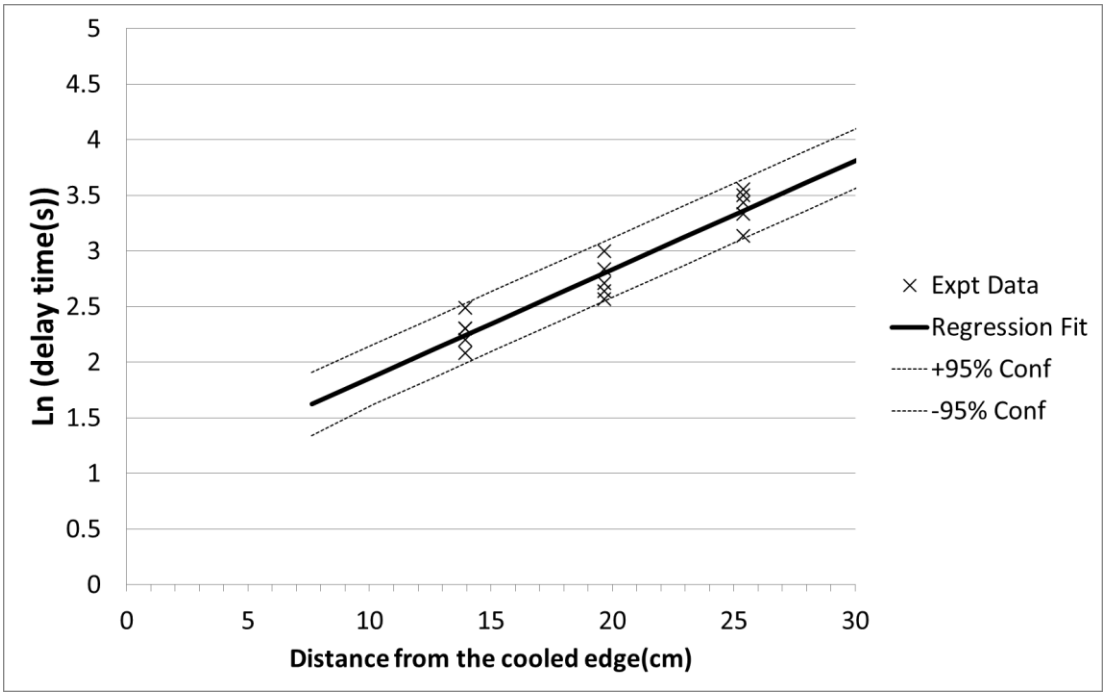

Figure 45: Regression fit showing 95 % confidence interval for delay time versus distance from cooled edge plot

5.3.2 Determination of jet spacing and timing

The samples from the conventionally cast and HiPerMag cooled cast plate were cut, mounted, polished, etched and analyzed according to scheme presented in section 4.3.4. The following figures (Figure 49, 50 and 51) show the micrographs for the conventionally cast plate, jet starting temperature of 600 °C and jet starting temperature of 620 °C plates. The distances shown in Figures 50, 51 and 52 are measured from the cooled edge of the plate as shown in Figure 41.

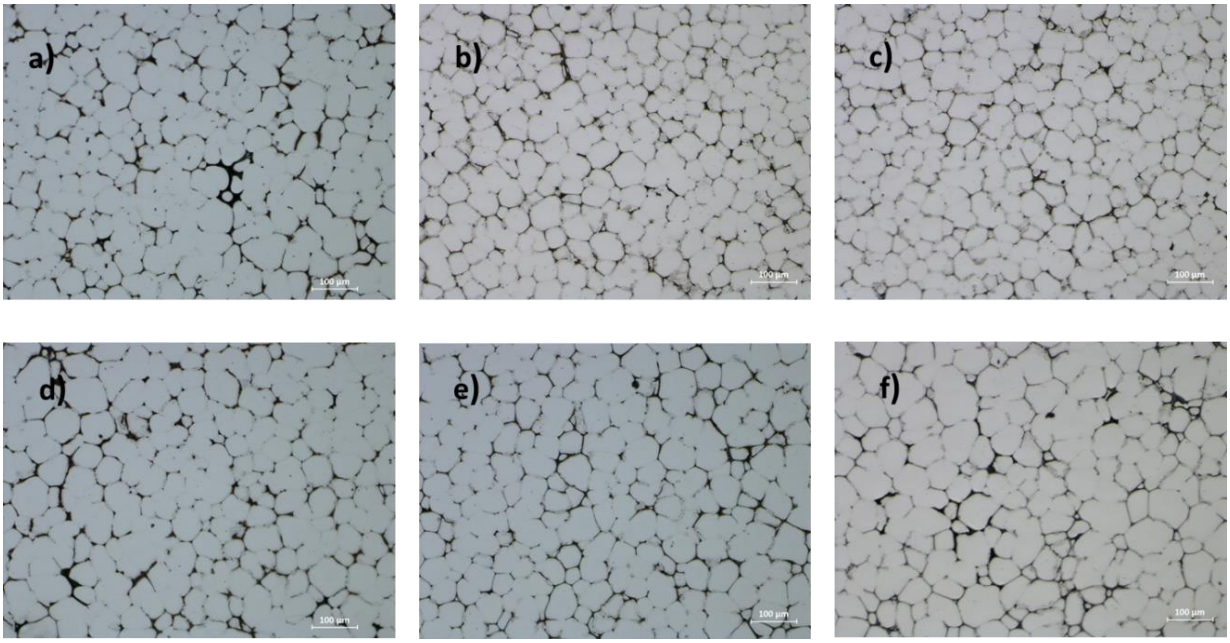

Figure 46: Microstructure of conventionally cast plate with distances from the cooled edge in cm at 100x (Keller's etch) a) 0 b) 3.8 cm c) 6.4 cm d) 8.9 cm e) 11.4 cm f) 14.0 cm

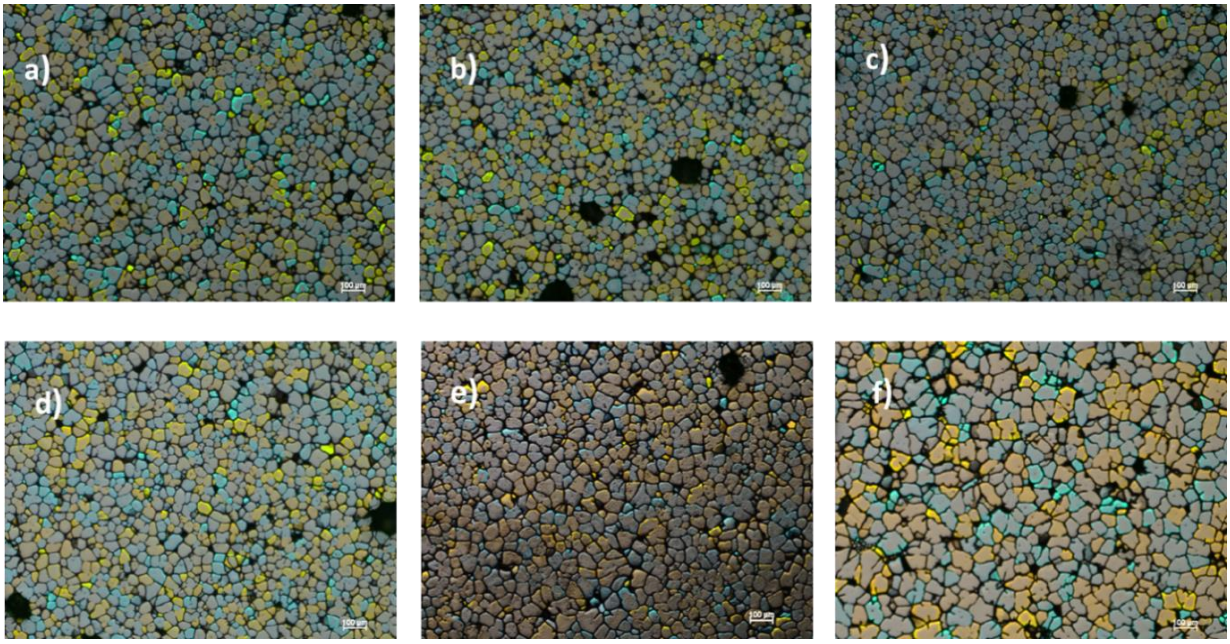

Figure 47: Microstructure of 600°C jet starting temperature plate with distances from the cooled edge in cm at 100x (Barker's etch) a) 0 b) 3.8 cm c) 6.4 cm d) 8.9 cm e) 11.4 cm f) 14.0 cm

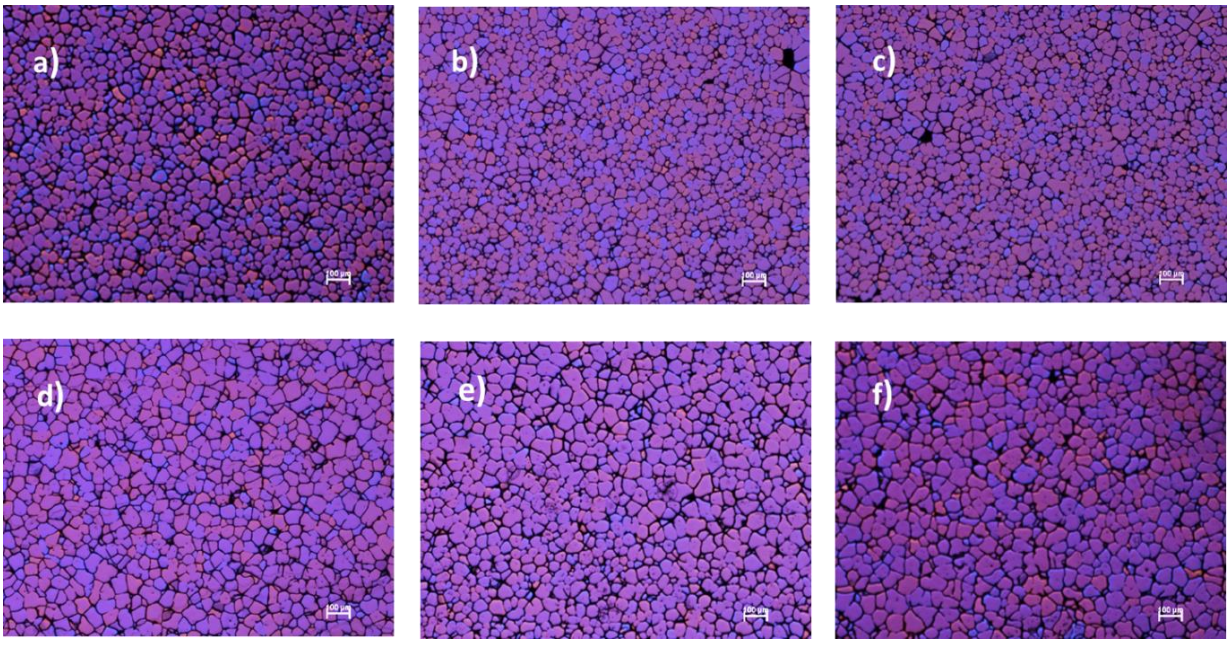

Figure 48: Microstructure of 620°C jet starting temperature plate with distances from the cooled edge in cm at 100x (Barker's etch) a) 0 b) 3.8 cm c) 6.4 cm d) 8.9 cm e) 11.4 cm f) 14.0 cm

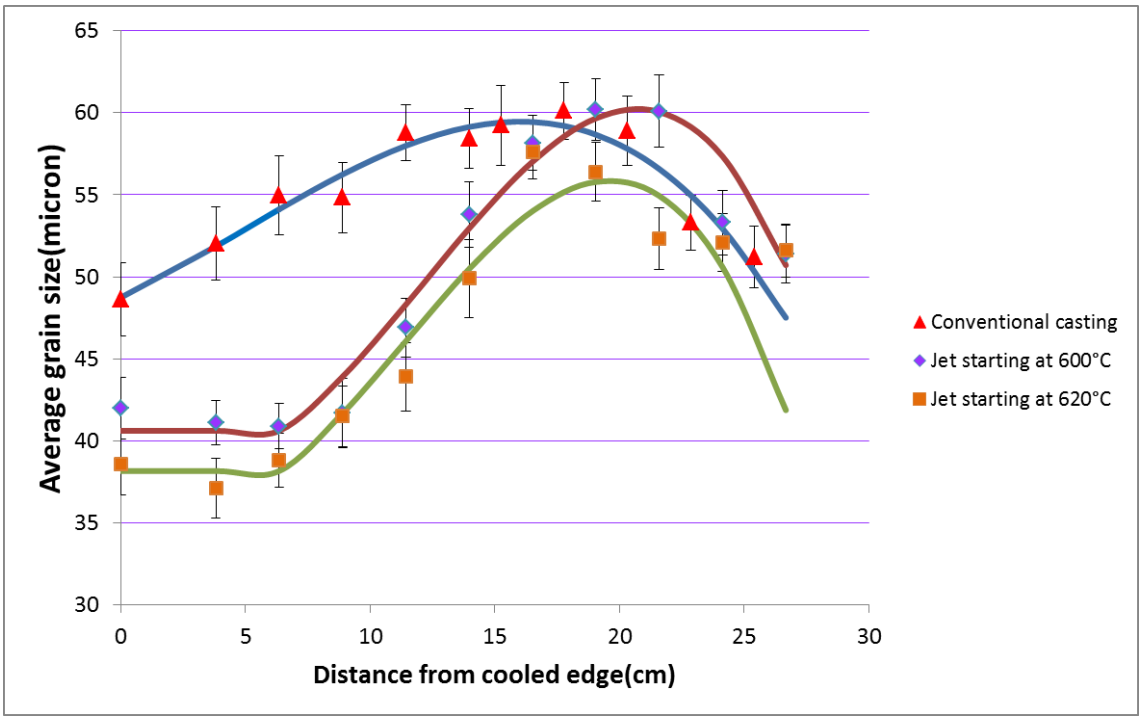

Figure 49: Average grain size vs. distance from the cooled edge for the three experimental conditions of conventional casting, starting the HiPermag jet at 600°C and 620°C

It can be observed from the average grain size plot (Figure 49) that the grain size variations started to exceed the 10 µm limit at a distance of about 11.4 cm from the cooled edge in all cases. This means the first water jet acted upon a region 8.9 cm from TC5 or 3.2 cm from TC6 for the grain size variation to remain in the tolerance level. This position will be referred henceforth as the "critical distance" as shown by point "Q" in Figure 51. Furthermore, the time for the solidification front to reach the critical distance, was be determined to be approximately 7.4 s as shown in Figure 50. From these plots, it was determined that the second jet should impinge on the plate when the solidification front reached point Q in order to maintain single solidification front

throughout the part. Since the coverage of each jet is approximately 12.7 cm, the maximum spacing between first and second jet should be set at approximately 15.3 cm (8.9 cm + 6.4 cm or half of the jet width). Also, it was concluded that the second jet should be started approximately 7.4 s after the start of the first water jet, as shown in Figure 50 and shown schematically in Figure 51.

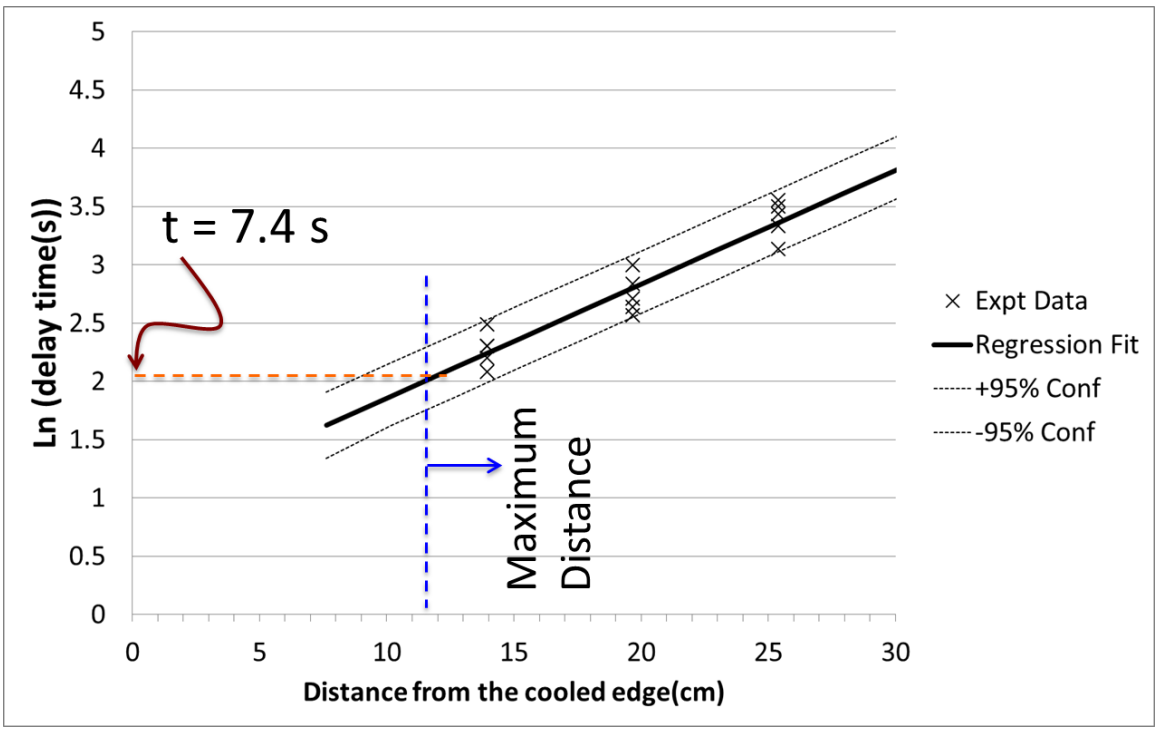

Figure 50: Determination of jet activation timing

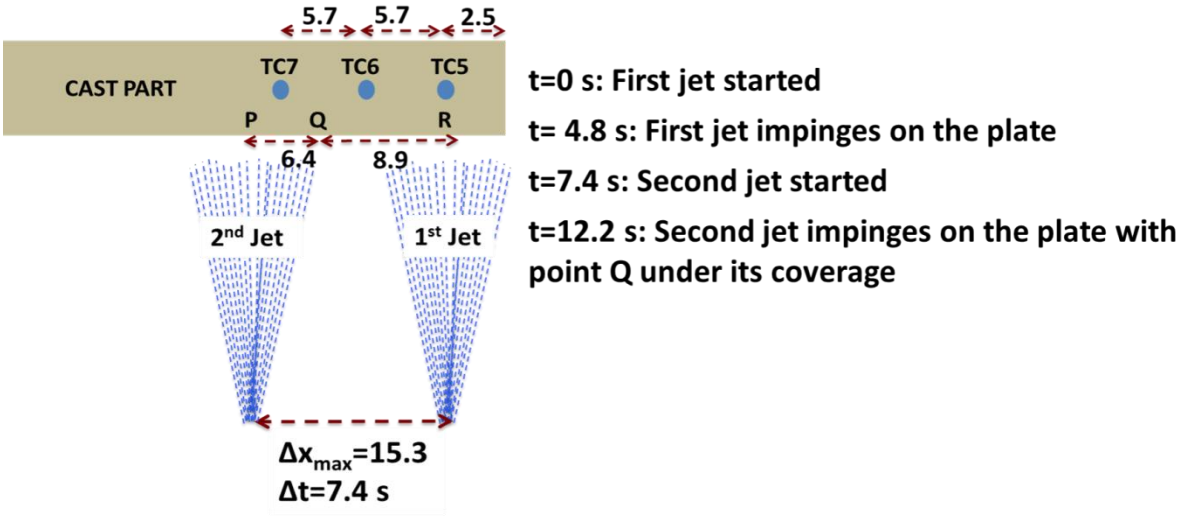

Figure 51: Jet activation timing and spacing schematic (all dimensions in cm)

It was mentioned above that the region under the jet impingement zone solidified as a single mass, as shown by the cooling curves for the thermocouples TC5 and TC6 in Figure 42 and Figure 43. Hence, it is preferred to have certain degree of overlap between first and second water jets to ensure that the entire jet impingement region solidified as a single mass without multiple solidification fronts being initiated. In such a case the jets can be started at the same time based on a particular jet starting temperature, obtained from surface defect curve to be discussed in the next section so that the entire part is quenched at a particular temperature, thus leading to a uniform grain size and mechanical properties for the casting.

In view of the literature on hot tearing (section 2.3), the high cooling rates present in the HiPerMag casting process are expected to increase the hot tearing tendency of the

casting. However, no hot tearing was observed in the present study. This may be due to the addition of grain refiner Ti, which might have offset the increase in tendency due to the higher cooling rate.

5.3 Determination of critical jet momentum for no surface defects

In this section, the effect of jet momentum on the surface integrity of the cast plate will be examined.

It is accepted that in order to obtain maximum grain refinement and high mechanical properties, the casting should be quenched with a jet momentum as high as possible with a starting temperature close to the liquidus. However, if the jet momentum is too high, the jet will damage or puncture the casting, rendering it useless. To establish a safe operating limit for the range of jet momentums to avoid damage to the part, a series of experiments were carried out with varying momentums (i.e. from 0.627 kg.m/s to 5.018 kg.m/s). Figure 52 shows the data points obtained in these plate-casting experiments.

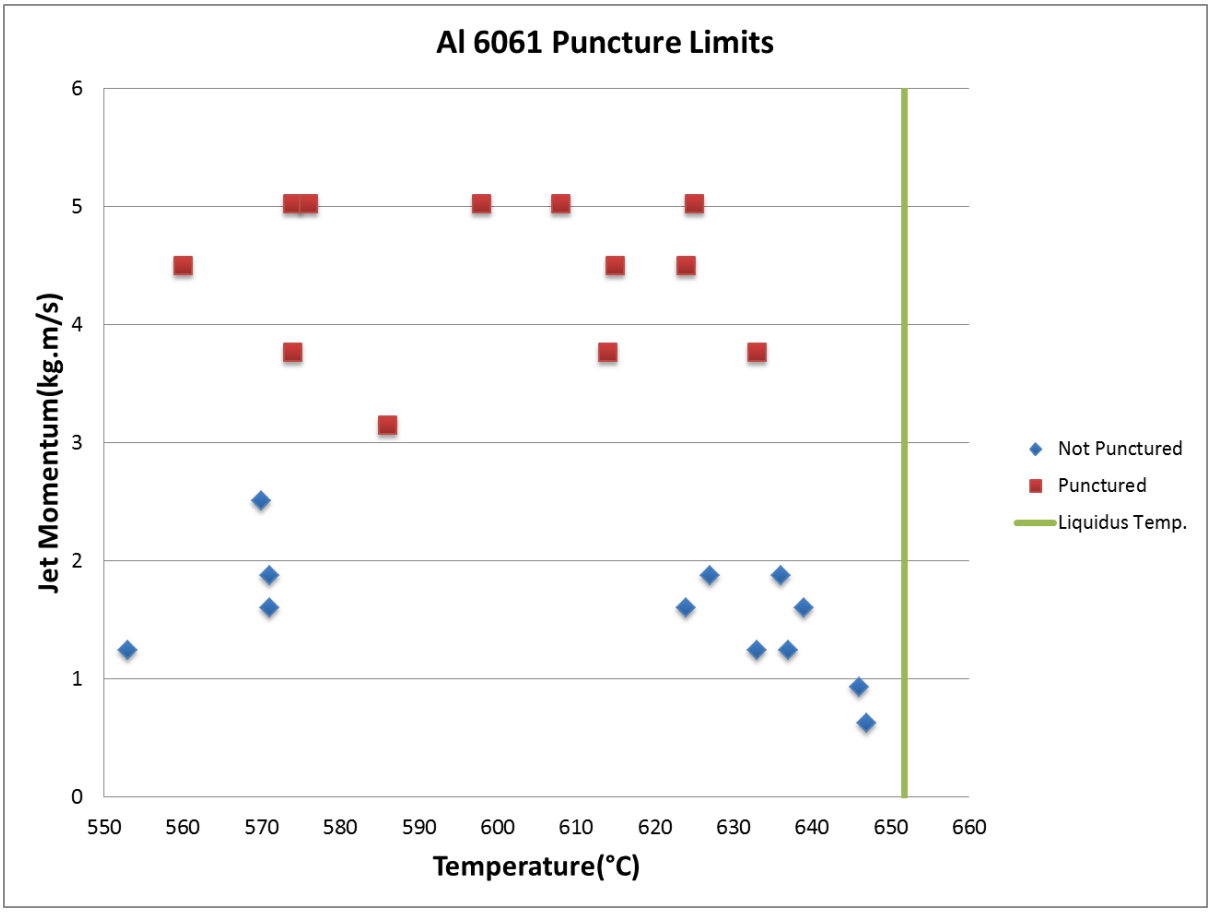

Figure 52: Surface defect curve

It is evident from Figure 52 that for water jet momentums higher than 3.0 kg.m⁄s results in surface defects regardless of the temperature of impingement (measured at TC5). Thus, a relatively low momentum (< 2.0 kg.m⁄s) can be used to successfully quench the part near the liquidus temperature as shown in bottom right corner of Figure 52.

Chapter 6: SUMMARY, CONCLUSIONS AND FUTURE WORK

6.1 Summary and Conclusions

This thesis highlights the complexities involved in the casting of a thin walled part by the HiPerMag casting process and provides process strategies for successfully implementing this process. The study was divided into three major parts that dealt with the optimization of the mold wall thickness, jet parameters, the minimization of grain size variation in the microstructure and the process parameters required to obtain a part free of surface defects arising from impingement of the water jet on the casting.

The study started with an evaluation of the properties of the sand binder system to ensure they met the molding requirements. An average green strength of 160 kPa and an average dry strength of 3825 kPa were found for the water soluble sand binder system used in the study. Also, for the alphaset bonded sand, an average tensile strength of 344 kPa was found at an interval of ten minutes after the strip time. These values were similar to those reported in the literature and were sufficient for making molds used for casting in the current study.

Secondly, a heat transfer model was developed to find the minimum mold thickness required to design a mold for the HiPerMag casting process such that the liquid metal remained sufficiently insulated before being quenched by the water jet. From the model, it was determined that for a cope thickness of 12.9 cm, the heat flux losses from the mold to the surrounding ambient air were reduced by up to 90 % versus a mold of a lower thickness. In addition, an analytical solution was derived for the mold thickness problem from which it was found that at a distance of 10 cm from the mold cavity there was a negligible increase in temperature of the sand mold at that location even at large times. Also, in this study, the minimum mold thickness was determined based on the temperature profile in the sand mold during the HiPerMag casting process. This study showed that a very thin mold of about 2 cm thickness was sufficient to provide insulation to the hot metal during the HiPerMag casting process.

The third part of the study sought to determine values of process variables such as the minimum jet spacing and jet activation timing based on casting cooling curve data and microstructural analysis. These two parameters are critical for casting any thin walled part of comparable thickness using the HiPerMag casting process. The jet spacing and timing were optimized to have a single solidification front throughout the part and which was necessary to avoid any hot tearing cracks (i.e. regions of high shrinkage with no liquid metal feed) arising from having multiple solidification fronts meeting. In addition, it was also ensured that the casting grain size variation remained below a cut-

off value of 10 µm in order to have uniform mechanical properties throughout the casting. Based on the cooling curve and microstructural analysis, a jet spacing of 15.3 cm and a jet activation time delay of 7.4 s between the successive jets starting from the farthest jet (located near the edge of the casting) was found. Also, from this study, it was found that the amount of solid present in the solidifying casting at the time of water jet impingement had a negligible effect on the solidification front velocity.

Lastly, a study on the effect of jet momentum on surface defects was carried out. It was found that there was a critical momentum below which there were no surface defects in the casting for impingement temperatures near the liquidus. For AA 6061 alloy this value was found to be 2 kg.m/s.

6.2 Future work

1. Investigate the effect of sand mold thickness on the cooling rate of the casting and grain size.
2. Conduct a permeability test for the current sand binder system.
3. Carry out tensile tests for plate casting samples.
4. Measure the amount of gas porosity in the HiPerMag cast samples and compare it to conventionally cast samples.
5. Study the effect of jet coverage on grain size.

6. Study the reclamation of the sand and water soluble binder to decrease the molding and consumable costs.

Chapter 7: REFERENCES

[1] D. Paxton, J. Carpenter, P. Sklad, M. Smith, "Overview of Lightweighting Materials R&D in the United States Freedomcar and Fuel Partnership" Materials Science Forum, vol. 618-619, pp. 395-404, 2009

[2] E. Ghassemieh, M. Chiaberge, "Materials in Automotive Application, State of the Art and Prospects, New Trends and Developments in Automotive Industry," 2011

[3] C.D. Goetz , E.C.Hathaway, H.R. Kottke, "Water soluble mold and core binders and method," Patent no: US 3046147 A, 1962

[4] "Clay Types Study Guide," (n.d.) Retrieved 21st Jan 2016 from http://culter.colorado.edu/~kittel/ClayTypesStudyGuide.ppt.

[5] "Sodium Bentonite: Its Structure and Properties," (n.d.) Retrieved 18th January 2016 from http://www.cetco.com/DesktopModules/Bring2mind/DMX/Download.aspx?Command=Core_Download&PortalId=0&EntryId=538

[6] R. E. Grim, *Clay Mineralogy*, 2nd Ed., McGraw Hill Book Company, New York, 1968

[7] C. Wenninger and W. Lang, "Sand Bentonite Water research and basic clay water concepts" AFS Trans., pp. 39-44, 1969

[8] K. Fuenkajorn, J.J. Daeme, "Sodium Bentonite as a Borehole Sealant" in *Sealing of Boreholes and Underground Excavations in Rock*, 1st Ed., London, UK, Chap. & Hall, 1996 p. 284

[9] P. Newcombe, CanMaterials, Hamilton, personal communication, January 2014

[10] H. S. Bawa, "Foundry" in *Manufacturing Processes – II*, New Delhi, India 2004, Tata McGraw Hill, 2004 , ch. 2,pp. 27-28

[11] Ahmad K. Elshennawy, Gamal S. Weheba, "Metal Casting Expendable Molds" in *Manufacturing Processes & Materials*, 5th Ed., Dearborn, 2015, SME, ch. 9, pp. 177-178

[12] R. W. Heine, E. H. King, and J.S. Schumacher, "Green Tensile and Shear Strengths of Moulding Sands," AFS Trans., vol. 67, pp. 229-236, 1959

[13] R. W. Heine, E. H. King, and J.S. Schumacher, "Correlation of Green Strength, Dry Strength and Mold Hardness of Molding Sands" AFS Trans., vol. 66, pp. 59-68, 1958

[14] J. Grassi, J. Campbell, M. Hartlieb and F. Major, "The Ablation Casting Process," Materials Science Forum, vol. 618, pp. 591-594, 2009

[15] J. Grassi, J. Campbell, F. Mayor, "Solidification Microstructure of Aggregate Molded Shaped Castings," US. Patent No. 2008⁄004149A1, Feb. 2008

[16] V. Bohlooli, M. Shabani, S. Boutorabi, "Effect of Ablation Casting on Microstructure and Casting Properties of A356 Aluminum Casting Alloy," Acta Metallurgica Sinica (E.L.), vol. 26, pp. 85-91, 2013

[17] D. Weiss, J. Grassi, B. Schultz, P. Rohatgi, "Ablation of Hybrid Metal Matrix Composites," American Foundry Society, pp. 26-29, Dec. 2011

[18] P. Rohatgi, "Casting Characteristics of Hybrid (Al/SiC/Gr) Composites," AFS Transactions, vol.19, pp. 191-197, 1998

[19] D. Weiss, J. Grassi, B. Schultz, P. Rohatgi, "Metal Casting Design and Purchasing," pp. 37-39, Jan-Feb 2012

[20] M. Tiryakioglu, Paul D. Eason, J. Campbell, "Fatigue life of ablation-cast 6061-T6 Components," Journal of Material Science and Engineering A, vol. 559 pp. 447-452, Jan.2013

[21] T. J. Williams, D. Galles, and C.Beckermann, "Translating Water Spray Cooling of a Steel Bar Sand Casting," in Proceedings of the 67th SFSA Technical and Operating Conference, Chicago, IL , paper no. 5.4 , 2013

[22] "Feeding & Risering Guidelines for Steel Castings," (n.d.) Steel Founders' Society of America, Barrington, Illinois, 2001 Retrieved 18th January 2016 from http://user.engineering.uiowa.edu/~becker/documents.dir/redbook.pdf

[23] A. Prescenzi, "Cast Body Nodes for 2016 Acura NSX," *SAE Int. J. Mater. Manf.* 8(3):722-730, 2015 (doi:10.4271/2015-01-0512)

[24] W. I. Pumphrey and P. H. Jennings, "A Consideration of the Nature of Brittleness at Temperature above the Solidus in Castings and Welds in Aluminum Alloys," J. Inst. Metals, vol. 75, pp. 235., 1948

[25] W.S. Pellini,"Strain Theorv of Hot Tearing," The Foundry, 80, (1952), pp. 124-199

[26] H.F. Bishop, C.G. Ackerlind, W.S. Pellini, "Metallurgy and Mechanics of Hot Tearing," Trans. AFS, vol. 68, pp 818-833, 1960

[27] J.C. Borland," Generalized Theorv of Super-Solidus Cracking in Welds (and Castings)", British Welding Journal, vol. 7, no. 8, pp. 508-512, 1960

[28] D.C.G. Lees, "The Hot Tearing Tendencies of Aluminium Casting Alloys", J. Inst. Metals, 72, (1946), p. 343-364

[29] H.F. Bishop, C.G. Ackerlind, W.S. Pellini,"Metallurgy and Mechanics of Hot Tearing", Trans. AFS, vol 68, pp 818-833, 1960

[30] S. Lin, C. Aliravci, M. Pekguleryuz, "Hot-Tear Susceptibility of Aluminum Wrought Alloys and the Effect of Grain Refining", Metallurgical and Materials Transactions A, vol. 38, Issue 5, pp. 1056-1068, 2007

[31] J. Langlais, "Fundamental Study of Hot Tearing Mechanisms of Aluminium silicon alloys", PhD dissertation, Dept. of Mining, Metals and Materials Eng., McGill University, Montreal, 2006

[32] M. Easton, J. F. Grandfield, D. H. St John, B. Rinderer, "The Effect of Grain Refinement and Cooling Rate on the Hot Tearing of Wrought Aluminum Alloys", Materials Science Forum, vol. 30, pp. 1675-1680, 2006

[33] L. Bichler, "Phenomenological studies of hot tearing during solidification of magnesium alloys", PhD dissertation, Dept. of Mech. Eng., Ryerson University, Toronto, 2009

[34] S.G. Shabestari, M.H. Ghoncheh, "Investigation on the Effect of Cooling Rate on Hot Tearing Susceptibility of Al2024 Alloy Using Thermal Analysis" Metall and Materi Trans B vol. 46, pp. 2438-2448, 2015

[35] A. Dursun, "Experimental Investigation of Sand Removal In Water-Soluble Sand Molds," MASc. thesis, Dept. of Mech. Eng., McMaster University, Hamilton, July 2015

[36] J. Campbell "Flow" in *Complete Casting Handbook: Metal Casting Processes, Metallurgy, Techniques and Design*, 2nd Ed., Oxford, UK, Butterworth-Heinemann, 2015 ch. 3, p. 98

[37] "Flat Spray Nozzles" (n.d.) Retrieved May 26th 2015 from: http://www.spray.com/cat75/hydraulic/files/71.html

[38] G. E. Totten, D. S. MacKenzie, *Handbook of Aluminum,* Volume 2, New York, Marcel Dekker, 2003, Appendix 3A, p. 713

[39] ASTM E112-13, " Standard Test Methods for Determining Average Grain Size" ASTM International, West Conshohocken, PA, 2013 (doi:10.1520/E0112)

[40] G. H. Geiger, D. R. Poirier, "Solidification Heat Transfer" in *Transport Phenomena in Metallurgy*, Addison-Wesley, 1973, ch. 10, pp. 329-330

[41] D. Stefanescu, "Macro Energy Transport" in *Science and Engineering of Casting Solidification,* 2nd Ed., New York, Springer,2009, ch. 5, pp. 81-85

[42] P. Newcombe, CanMaterials, Hamilton, personal communication, January 2015

[43] Y. Nishida, W. Droste, and S. Engler: Metall. Trans. B, 1986, vol. 17B, pp. 833–44

[44] W.D. Griffiths, Metall. Mater. Trans. B, 1999, vol. 30B, pp. 473–82

[45] "Thermal Conductivity of some common Materials and Gases" (n.d.) http://www.engineeringtoolbox.com/thermal-conductivity-d_429.html, Retrieved 1st July 2016

[46] J. Lienhard lV, J. Lienhard V, "Introduction" & "Heat conduction concepts, thermal resistance and the overall heat transfer coefficient" in *A Heat Transfer Textbook* , 3rd Ed., Cambridge, Phlogiston Press, 2008, ch. 1 & 2

[47] L. Chen, Y. Wang, L. Peng, P. Fu,H. Jiang, "Study of interfacial heat transfer coefficient between AZ91D magnesium alloy and silica sand," Experimental Thermal and Fluid Science, vol. 54, pp. 196-203, 2014

[48] R. Ajdar, "Effect of mold materials on solidification, microstructure and fluidity of A356 alloy in lost foam casting" MASc. thesis, Dept. of Material Sc. & Eng., Univ. of Toronto, Toronto, 2001

[49] A. Sharma, "Mold cavity layout optimization in sand casting," M.Tech. dissertation , Dept. of Mech. Eng., IIT-Bombay, Mumbai, 2009

[50] "Bending Stresses for Simple Shapes," (n.d.) Retrieved 15th July 2015 from www.atcpublications.com/Sample_pages_from_FDG.pdf:

[51] "Beam Deflection, Stress Formula and Calculators," (n.d.) Retrieved 15th July 2015 from http://www.engineersedge.com/beam_bending/beam_bending1.htm